MOLECULAR SOLVATION DYNAMICS FROM INELASTIC X-RAY SCATTERING MEASUREMENTS

R. H. CORIDAN[1] and G. C. L. WONG

Department of Bioengineering, Department of Chemistry and Biochemistry, and California NanoSystems Institute, University of California, Los Angeles, CA 90024, USA

CONTENTS

---

[1] Current address: Division of Chemistry and Chemical Engineering, California Institute of Technology, Pasadena, California, 91125

I.   INTRODUCTION

Water's interactions with other molecules are what make it an important liquid in chemistry and biology. The overall neutral water molecule carries fractional positive charges on its hydrogen atoms and a negative charge on its oxygen, giving the molecule a strong dipole moment. Water molecules donate or accept electron density to form strongly oriented hydrogen bonds with ions. The direction of charge transfer depends on the sign of the overall ionic charge. Water has also strong electrostatic interactions with polarizable solutes and reorganizes its hydration structure around changes in solute charge density. Examples of the importance of solvation interactions in water are numerous.

At an interface, hydration depends on the surface's structure and chemical composition. Some metals such as platinum can break covalent bonds in water molecules [1]. Hydrophilic surfaces interact so strongly with interfacial water that the local viscosity can increase many orders of magnitude in the first molecular layers [2, 3], while possessing near bulk fluidity in subsequent layers [4, 5]. At present, the dynamics and structure of water at hydrophobic surfaces [6–8] is still being debated.

Chemical reactions are regulated by the hydration environment surrounding nearby reactants. Electron transfer occurs in redox pairs when the surrounding water molecules fluctuate to a configuration that facilitates the exchange [9]. The wide range of effects different ions have on the structure of solvent water has strong implications on the solubility of proteins. This little understood phenomenon is known as the Hofmeister effect [10].

Protein structure and function is dominated by its interaction with water. A protein's function is defined by its amino acid side groups, which have different shapes, sizes, and degrees of hydrophobicity or hydrophilicity. The way a protein folds, catalyzes chemical reactions, and interacts with other proteins strongly depends on its interaction with water. The structure and dynamics of the interfacial water affect the protein's stability and function [11]. On larger scales, macromolecular self-assembly is driven by hydrophobic and amphiphilic interactions. Biological structures from membranes [12] to amyloid fibrils [13] are the consequence of water–molecule interactions.

The static structure and hydrogen bonding network of liquid water is investigated by scattering and absorption experiments. X-ray and neutron scattering measure the intermolecular pair correlation functions of water that describe the distribution of water molecules relative to each other [14, 15]. Neutron

scattering can also discriminate between atomic pairs to yield the correlation functions for pairs of atoms (H–H, O–O, and O–H) due to its high sensitivity to hydrogen atoms [16]. These functions elucidate the relative positions and orientations of water molecules in the bulk. X-ray absorption spectroscopy probes the local hydrogen bonding environment of water in different thermodynamic conditions by comparing measured absorption spectra to that for ice [17, 18]. In solute–solvent systems, neutron scattering has also been utilized to reconstruct the static three-dimensional hydration structure around small molecules, such as methanol [19] and noble gases like krypton [20], by measuring the concentration dependence of the interatomic pair correlation functions. The effect ions in solution have on the hydrogen bonding network of water has been studied by XAS measurements as well [21].

Pump-probe IR spectroscopy provides sufficiently high resolution to determine the molecular dynamics of water. Femtosecond resolution is important to these measurements because virtually all molecular-scale dynamical processes in water occur on timescales of tens of femtoseconds to a few picoseconds. The ability to create distinct pulses of IR radiation that are separated by tens of femtoseconds allows the observation of these processes. This technique has been used to measure fundamental dynamics in water, such as orientational lifetimes of water molecules [22] and the dynamics energy transfer through the hydrogen bond network [23]. The bond length dependence of a mode's IR absorption allows it to be used as a "spectroscopic ruler" to observe the hydrogen bond O–O oscillation period in water [24]. For solute–solvent systems, pump-probe experiments dynamically monitor the characteristic absorption frequencies of different modes in the presence of ions and other molecules. Other experiments excite the electronic state of the solute molecule itself and monitor the dynamical response of the surrounding solvent. A solute molecule, such as a chromophore, can be photoexcited or photoionized to change its underlying charge structure. An absorption or pump-probe experiment then determines the changes in the solvent's IR spectra in response to the change in solute charge density [25–27].

While experimental techniques have provided many high-resolution measurements of static or dynamical properties of water, achieving high resolution in one category has typically meant poorly resolved measurements in the other. X-ray scattering can measure the pair correlation function of water to sub-Å resolution, but it integrates over a large sample volume and measurement times much larger than molecular timescales. The result is a time-averaged structure. Likewise, measurements of the intermolecular hydrogen bond oscillation give little information about the intermolecular structure of water on these timescales. For the most part, one is forced to choose between high temporal and high spatial resolution.

Inelastic X-ray scattering (IXS) is a hybrid scattering and spectroscopic technique that simultaneously measures structural and dynamical properties of

Figure 1. Collective modes in water have been previously measured using IXS. In this 1996 measurement, the sound mode was mapped out to $q = 14$ nm^{-1}. Reprinted with permission from Ref. [30]. Copyright 1996 by the American Physical Society.
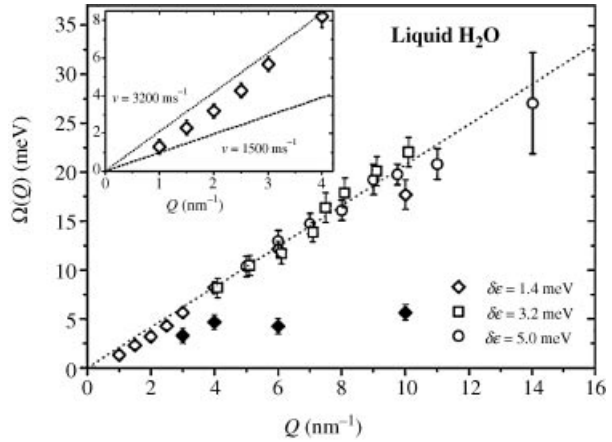
condensed systems. As in typical X-ray scattering, the momentum transfer to the system is determined by the scattering angle between the incident and scattered photons. In addition, IXS incorporates spectroscopic discrimination to measure the energy gain or loss of scattered photons. IXS spectra are measurements of the dynamical structure factor $S(q, \omega)$. Because momentum and energy transfer are conjugate variables of spatial and temporal periodicity, respectively, $S(q, \omega)$ is the time and space Fourier transformed measure of density fluctuations in a system. High-intensity third-generation synchrotron X-ray sources have enabled the development of meV-resolution IXS spectrometers that can measure atomic density–density correlation functions. These instruments have been used to the study of collective modes in liquid water (Fig. 1), which has demonstrated that water behaves more like a solid than a liquid on short length scales [28]. It has also shown that these density fluctuations are due to center of mass motions rather than bond or rotational motions [29, 30].

Abbamonte et al. [31] established that a full measurement of $S(q, \omega)$ in water can be "inverted" to recover the density response function $\chi(q, \omega)$, which quantifies the effect of an external perturbation on the surrounding hydration medium. The inversion requires a solution to a phase problem that only the imaginary part of $\chi(q, \omega)$ is directly related to $S(q, \omega)$. They demonstrated that Kramers–Kronig (KK) relations are the solution to this phase problem and can be used to recover the real part from IXS measurements. The full complex-valued $\chi(q, \omega)$ was Fourier transformed to produce the time and space density response function $\chi(r, t)$. In linear response (LR), $\chi(r, t)$ is a Green's function that facilitates the imaging of the induced charge density in water surrounding model charge distribution. The transferred energies measured in this work were on the scale of electron volts (eV), corresponding to the attosecond (10^{-18} s, resolution related to energy by

$\Delta t = \pi \hbar / E_{max}$) dynamics of electronic excitations. They used the recovered response function to image the response around model charge densities, similar to an ideal chromophore and a relativistic heavy ion.

Here, we review the application of Kramers–Kronig relations to meV-resolution IXS measurements of $S(q, \omega)$ to extract the density–density response function $\chi(q, \omega)$. For this energy range, $S(q, \omega)$ describes the spectrum of atomic density fluctuations in a system. Assuming that the transferred energy is small enough to leave the molecular electron density unperturbed (the *adiabatic* approximation), $S(q, \omega)$ reflects the spectrum of fluctuations of charge density in a medium [32]. IXS can be used to measure the meV-resolution dynamic structure factor of liquid water and invert it to recover the density response function $\chi(q, \omega)$ for dynamics on femtosecond (10^{-15} s) timescales. $S(q, \omega)$ can be measured to sufficiently high energy ($E_{max} = 80$ meV) and momentum transfers ($q_{max} = 7.2$ Å^{-1}) to attain 26 fs temporal and 0.5 Å spatial resolution for the inverted Green's function. This can be used in the same linear response formalism to image the hydration structure around dynamical charge densities in water for time and length scales corresponding to molecular motion and structure. Though the general protocol is similar to the eV-scale studies, the profile of $S(q, \omega)$ and the underlying physical processes are very different and require special experimental consideration.

In Section II, we review the theoretical definitions of the dynamic structure factor $S(q, \omega)$ and the density response function $\chi(q, \omega)$ with respect to scattering. The Kramers–Kronig relations are derived in this context as well. We also present the general features and experimental considerations of an meV-IXS instrument. In Section III, we detail the inversion of an extensive measurement of the meV-scale dynamical structure factor of liquid water, complete with discussion on how to treat the data for experimental artifacts. The results of "proof of concept" diagnostic tests of the measured $\chi(r, t)$ are described, and the results are compared with other static and dynamical direct measurements. We also show how $\chi(r, t)$ can be used as a Green's function to reconstruct femtosecond movies of the dynamical hydration structure around a prototypical moving charge in water. To reconstruct the solvation structure around realistic ionic and molecular solutes, a simple implementation of excluded volume is proposed in Section IV. Static and dynamical calculations are compared with the results of simulations and measurements. Finally, we consider the range of validity of the GFID technique. We examine systems in which linear response theory fails and discuss potential directions for improving it.

II. REVIEW OF HIGH-RESOLUTION INELASTIC X-RAY SCATTERING ON LIQUID WATER: THEORY AND EXPERIMENT

IXS measures the spectrum of density fluctuations in condensed matter systems, such as liquids and solids. Excitations such as phonons and plasmons can be

observed by selecting the appropriate energy and momentum transfer ranges for observation [33, 34]. The arrival of intense third-generation synchrotron X-ray sources has made high-resolution ($\Delta E \approx 1$ meV) IXS feasible, in part due to the narrow bandwidth required for such measurements. For example, the energy resolution of IXS measurements was insufficient to observe the low energy transfer characteristic of phonon modes ($\sim$10–100 meV) in crystals until the early 1980s [35] and the resolution required to observe collective modes ($\Delta E \approx 1$ meV) in liquids was not achieved until the mid-1990s [29].

There are many reviews of inelastic scattering as a technique to study a broad range of elementary excitations in condensed matter systems [33, 34, 36–38]. Here, we introduce the physics of IXS with an emphasis on meV-resolution experiments used to observe collective modes in disordered systems such as liquids. We include a brief discussion of a high-resolution IXS instrument.

A. Static Structure from Elastic X-Ray Scattering Experiments

Typical X-ray scattering experiments measure the intensity of X-rays scattered by a sample as a function of the momentum transferred to the system. The measured quantity is the scattering intensity $I(\mathbf{q})$, a function of the momentum transfer $\mathbf{q}$. Momentum is the conjugate variable of position, so $I(\mathbf{q})$ yields information about the relative positions between scatterers (atoms, molecules, etc.) in the sample. An X-ray of initial momentum $\mathbf{k}_i = (2\pi/\lambda)\hat{k}_i$ is scattered by a sample to a final momentum $\mathbf{k}_f$. The momentum transfer $\mathbf{q}$ is the difference between these, $\mathbf{k}_f - \mathbf{k}_i$. The convention for describing scattering processes is illustrated in Fig. 2. For studies of static structure, elastic scattering is employed, so the magnitude of the initial and final momenta, and therefore the wavelength, is conserved:

$$|\mathbf{k}_f| = |\mathbf{k}_i| = \frac{2\pi}{\lambda} \tag{1}$$

The magnitude of $\mathbf{q}$ (to be referred to as q) is then determined by λ and the scattering angle θ_{sc},

$$q = 2k_i \sin \frac{\theta_{sc}}{2} = \frac{4\pi}{\lambda} \sin \frac{\theta_{sc}}{2} \tag{2}$$

Figure 2. An X-ray with initial momentum $\mathbf{k_i}$ is incident on a sample and scattered by an angle θ_{sc} to a final momentum $\mathbf{k_f}$. The momentum transferred to the sample is $\mathbf{q} = \mathbf{k_i} - \mathbf{k_f}$.
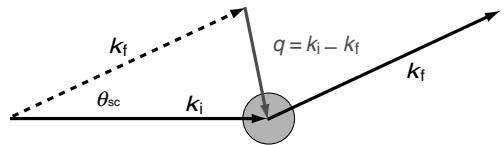
The scattered intensity for bulk atomic and molecular systems is proportional to the product of the square of the form factor $F(\mathbf{q})$ and the structure factor $S(\mathbf{q})$ [37, 39],

$$I(\mathbf{q}) \propto |F(\mathbf{q})|^2 S(\mathbf{q}) \tag{3}$$

$F(\mathbf{q})$ is the Fourier transform of the scattering potential of the basis scattering unit, similar to an assembly of atoms or a molecule.

In real space, the number density at a given position $n(\mathbf{r})$ is

$$n(\mathbf{r}) = \sum_{i=1}^{N} \delta (\mathbf{r} - \mathbf{r}_i) \tag{4}$$

where $\mathbf{r}_i$ is the position of the ith particle. $S(\mathbf{q})$ is the Fourier transform of the density–density correlation function

$$\langle \delta n(\mathbf{r}) \delta n(\mathbf{r}') \rangle = \langle [n(\mathbf{r}) - \langle n(\mathbf{r}) \rangle][n(\mathbf{r}') - \langle n(\mathbf{r}') \rangle] \rangle$$

where $\langle \ldots \rangle$ represents the ensemble average value. This is also the pair correlation function $g(\mathbf{r}, \mathbf{r}')$,

$$g(\mathbf{r}, \mathbf{r}') = \frac{\langle \sum_{\mathbf{r}_\alpha \neq \mathbf{r}'} \delta(\mathbf{r} - \mathbf{r}_\alpha + \mathbf{r}') \rangle}{\langle n \rangle} \tag{5}$$

which can be understood in the following way: given that there is a particle at $\mathbf{r}'$, $g(\mathbf{r}, \mathbf{r}')$ is the average number of particles at the position $\mathbf{r}$, excluding its self contribution [37]. Typically, $\mathbf{r}'$ is chosen to be the origin without loss of generality, and $g(\mathbf{r})$ is written only as a function of the position $\mathbf{r}$.

The structure of a crystal is determined by Bragg diffraction. With the assumption that scatterers are fixed at positions on a lattice, the interference between lattice planes causes the scattered intensity to be nonzero only in the neighborhood of specific values of $\mathbf{q}$ such that

$$\mathbf{r}_{hkl} \times \mathbf{q} = 2\pi \tag{6}$$

where $\{\mathbf{r}_{hkl}\}$ is the set of normal vectors defining the lattice planes. This can be understood from the definition of the pair correlation function in Eq. (5). For a given scatterer, there are discrete vectors at which another scatterer will be found. For a crystal, the set of momentum transfer vectors $\{\mathbf{q}_{hkl}\}$ that satisfy Bragg's law [Eq. (6)] are the reciprocal space representation of the crystal lattice [40, 41]. The measured intensity of scattered X-rays forms sharp peaks at the discrete q positions $\{\mathbf{q}_{hkl}\}$.

The scattered X-ray intensity is no longer comprised of sharp peaks for disordered systems like liquids. The scatterers are diffusively mobile and can be found
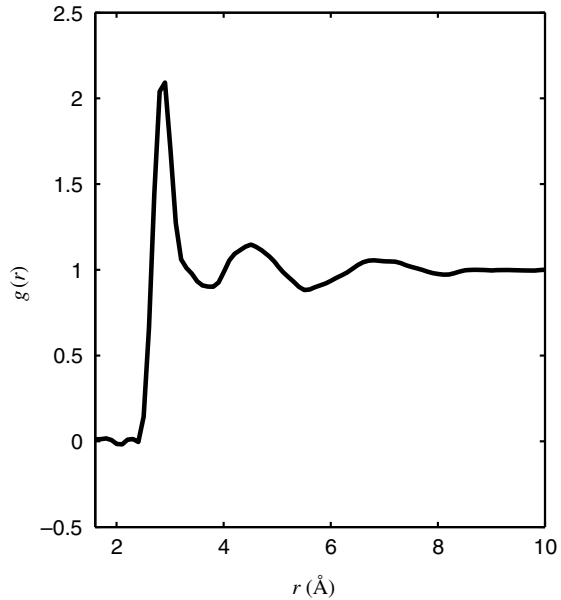
Figure 3. The static pair correlation function $g(r)$ of room-temperature liquid water. This example of $g(r)$ was calculated from data published in Ref. [42].

at any distance from one another. The pair correlation function $g(\mathbf{r})$, structure factor $S(\mathbf{q})$, and the scattered intensity $I(\mathbf{q})$ are also continuous and only show structure for length scales of a few molecular diameters. In isotropic liquids, these quantities depend only on the magnitude of the position or momentum vectors: $I(\mathbf{q}) \rightarrow I(q)$, $S(\mathbf{q}) \rightarrow S(q)$, and $g(\mathbf{r}) \rightarrow g(r)$. Figure 3 shows the pair correlation function $g(r)$ of room-temperature liquid water as calculated from published structure factor measurements [42]. The peaks in $g(r)$ correspond to hydration shells with the first found roughly 2.8 Å from the center of a given water molecule. For static X-ray scattering, the pair correlation function $g(r)$ is the most information that can be extracted experimentally.

B. Dynamic Structure from Inelastic X-Ray Scattering Experiments

Like momentum and position, energy and time are a pair of conjugate variables. IXS combines the momentum transfer measurements of static X-ray scattering with spectroscopic discrimination of scattered photons to measure the structure and dynamics of density fluctuations *simultaneously*. The energy loss or gain of a scattered photon provides information on the dynamics of the scatterers on the corresponding timescales. The measured intensity $I(\mathbf{q}, \omega)$ is proportional to the dynamical structure factor $S(\mathbf{q}, \omega)$, the time and space analogues of the static structure factor $S(\mathbf{q})$ previously introduced. $S(\mathbf{q}, \omega)$ describes the

spectra of correlated density fluctuations in a system and is the time and space Fourier transform of the time-dependent density–density correlation function $\langle \delta n(\mathbf{r} - \mathbf{r}', t - t')\delta n(\mathbf{r}', t')\rangle$ [36]. Liquid water is isotropic, so $S(\mathbf{q}, \omega) = S(q, \omega)$ and is the Fourier transform of the isotropic time-dependent density–density correlation function $\langle \delta n(|\mathbf{r} - \mathbf{r}'|, t - t')\delta n(|\mathbf{r}'|, t')\rangle$.

In this section, we introduce the concepts of the dynamic structure factor and linear response theoretically. This allows the direct derivation of their relationship to help clarify the procedure for recovering the linear response function $\chi(q, \omega)$ from measurements of $S(q, \omega)$. This discussion follows closely several seminal reviews on the topic [33, 34, 36, 37].

The quantum mechanical operator $\delta n_{\mathbf{q}}$ describes the Fourier component of the density $\delta n(\mathbf{r}) = n(\mathbf{r}) - \langle n \rangle$: $\delta n_{\mathbf{q}} = \sum_i e^{\imath \mathbf{q} \cdot \mathbf{r}_i}$, where the sum is over all particles in the system and $\mathbf{r}_i$ is the position of the ith particle. The time-dependent density operator $\delta n_{\mathbf{q}}(t)$ evolves according to the Hamiltonian $\hat{H}$, $\delta n_{\mathbf{q}}(t) = e^{\imath \hat{H} t} \delta n_{\mathbf{q}} e^{-\imath \hat{H} t}$. For a system at finite temperature T, the dynamic structure factor $S(\mathbf{q}, \omega)$ is the average over all possible initial and final states of the system $|i\rangle$ and $|f\rangle$, respectively. $S(\mathbf{q}, t)$ is defined as

$$
\begin{aligned}
S(\mathbf{q}, t) &= \sum_i \frac{e^{-\beta E_i}}{Z} \langle i | \delta n_{\mathbf{q}}^{\dagger}(t) \delta n_{\mathbf{q}}(0) | i \rangle \\
&= \sum_i \frac{e^{-\beta E_i}}{Z} \langle i | e^{-\imath \hat{H} t} \delta n_{\mathbf{q}}^{\dagger} e^{\imath \hat{H} t} \delta n_{\mathbf{q}} | i \rangle \\
&= \sum_i \sum_f \frac{e^{-\beta E_i}}{Z} \langle i | e^{-\imath \hat{H} t} \delta n_{\mathbf{q}}^{\dagger} e^{\imath \hat{H} t} | f \rangle \langle f | \delta n_{\mathbf{q}} | i \rangle \\
&= \sum_{i,f} \frac{e^{-\beta E_i}}{Z} e^{-\imath (E_i - E_f) t} \langle i | \delta n_{\mathbf{q}}^{\dagger} | f \rangle \langle f | \delta n_{\mathbf{q}} | i \rangle \\
&= \sum_{i,f} \frac{e^{-\beta E_i}}{Z} e^{-\imath \omega t} |(\delta n_{\mathbf{q}})_{fi}|^2
\end{aligned}
\tag{7}
$$

where E_i and E_f are the energies corresponding to states $|i\rangle$ and $|f\rangle$, and the energy transfer is defined as $\omega = (E_i - E_f)$. β is the inverse of temperature $(k_B T)^{-1}$. The prefactor $e^{-\beta E_i}/Z$ is the Boltzmann distribution probability that the system is in state $|i\rangle$, and $Z = \sum_i e^{-\beta E_i}$ is the partition function. From this definition of $S(\mathbf{q}, t)$, it is clear that it is the inverse Fourier transform of the dynamic structure factor $S(\mathbf{q}, \omega)$,

$$
S(\mathbf{q}, \omega) = \sum_{i,f} \frac{e^{-\beta E_i}}{Z} |(\delta n_{\mathbf{q}})_{fi}|^2 \delta(\omega - (E_i - E_f))
\tag{8}
$$

Transposing the initial and final states demonstrates an important property of $S(\mathbf{q}, -\omega)$,

$$
\begin{aligned}
S(\mathbf{q}, -\omega) &= \sum_{i,f} \frac{e^{-\beta E_f}}{Z} |(\delta n_{\mathbf{q}})_{fi}|^2 \delta(-\omega - (E_f - E_i)) \\
&= \sum_{i,f} e^{-\beta(E_f - E_i)} \frac{e^{-\beta E_i}}{Z} |(\delta n_{-\mathbf{q}})_{fi}|^2 \delta(-(\omega - (E_i - E_f))) \\
&= e^{-\beta \omega} S(-\mathbf{q}, \omega)
\end{aligned}
\tag{9}
$$

Because the scattering cross section is invariant for $\mathbf{q} \to -\mathbf{q}$,

$$
S(\mathbf{q}, -\omega) = e^{-\beta \omega} S(\mathbf{q}, \omega)
\tag{10}
$$

which is a statement of detailed balance. The relative probability that the system is initially in state $|i\rangle$ rather than in state $|f\rangle$ is the ratio of their Boltzmann factors, $e^{-\beta E_i}/e^{-\beta E_f} = e^{-\beta \omega}$.

A linear response theory assumes that the influence of a small perturbation on the system causes a response in the system that propagates through the fluctuation modes encapsulated by $S(q, \omega)$. The goal is to find a linear response function $\chi(\mathbf{q}, \omega)$ that relates the external perturbation $\phi(\mathbf{q}, \omega)$ to the induced density in the system $\delta n_{\text{ind}}(\mathbf{q}, \omega)$:

$$
\delta n_{ind}(\mathbf{q}, \omega) = \chi(\mathbf{q}, \omega)\phi(\mathbf{q}, \omega)
\tag{11}
$$

$\phi(\mathbf{q}, \omega)$ is assumed to be a real, scalar potential field that interacts with density fluctuations via a Hamiltonian of the form

$$
\hat{H} = e^{\zeta t}\left(\delta n_{\mathbf{q}}^{\dagger} \phi(\mathbf{q}, \omega) e^{-\iota \omega t} + \delta n_{\mathbf{q}} \phi(\mathbf{q}, \omega) e^{\iota \omega t} \right)
\tag{12}
$$

where the term $e^{\zeta t}$ enforces that the perturbation is "turned on" sufficiently slowly so as not to cause transitions in the system that will force it out of its unperturbed state, also known as the adiabatic approximation. ζ is assumed to be sufficiently small that the limit $(\zeta \to 0)$ can be taken in the end. It can be shown that the Hamiltonian describing interactions between electromagnetic fields and matter is of the form shown in Eq. (12) [34, 43].

Through first-order perturbation theory [36], it is shown that the linear response function $\chi(\mathbf{q}, \omega)$ is

$$
\chi(\mathbf{q}, \omega) = \sum_{i,f} \frac{e^{-\beta E_i}}{Z} |(\delta n_{\mathbf{q}})_{fi}|^2 \left\{ \frac{1}{\omega - \omega_{fi} + \iota \zeta} - \frac{1}{\omega + \omega_{fi} + \iota \zeta} \right\}
\tag{13}
$$

By utilizing the Dirac relation [36],

$$\lim_{\zeta \to 0} \frac{1}{x + \iota\zeta} = \mathcal{P}\left(\frac{1}{x}\right) - \iota\pi\delta(x) \tag{14}$$

the limit for $\chi(\mathbf{q}, \omega)$ can be taken for $\zeta \to 0$,

$$\chi(\mathbf{q}, \omega) = \sum_{i,f} \frac{e^{-\beta E_i}}{Z} |(\delta n_\mathbf{q})_{fi}|^2$$

$$\times \left\{ \left[\mathcal{P}\left(\frac{1}{\omega - \omega_{fi}}\right) - \iota\pi\delta(\omega - \omega_{fi}) \right] - \left[\mathcal{P}\left(\frac{1}{\omega + \omega_{fi}}\right) - \iota\pi\delta(\omega + \omega_{fi}) \right] \right\} \tag{15}$$

Equation (15) can be rewritten to express the response function as the sum of real and imaginary parts: $\chi(\mathbf{q}, \omega) = \chi'(\mathbf{q}, \omega) + \iota\chi''(\mathbf{q}, \omega)$, where

$$\chi'(\mathbf{q}, \omega) = \sum_{i,f} \frac{e^{-\beta E_i}}{Z} |(\delta n_\mathbf{q})_{fi}|^2 \left\{ \mathcal{P}\left(\frac{1}{\omega - \omega_{fi}}\right) - \mathcal{P}\left(\frac{1}{\omega + \omega_{fi}}\right) \right\} \tag{16}$$

and

$$\chi''(\mathbf{q}, \omega) = -\pi \sum_{i,f} \frac{e^{-\beta E_i}}{Z} |(\delta n_\mathbf{q})_{fi}|^2 \left\{ \left(\delta(\omega - \omega_{fi}) - \delta(\omega + \omega_{fi}) \right) \right\} \tag{17}$$

Combining Eqs. (8) and (17) provides an important result

$$\chi''(\mathbf{q}, \omega) = -\pi\{\mathbf{S}(\mathbf{q}, \omega) - \mathbf{S}(\mathbf{q}, -\omega)\} \tag{18}$$

This relationship between χ'' and S is a mathematical expression of the fluctuation-dissipation theorem, which states that for sufficiently small perturbations, the dissipative response in the system is carried out by the same modes that govern its equilibrium fluctuations. $\chi''(\mathbf{q}, \omega)$ is called the dissipative part of the response because it is proportional to the work done by the perturbation on the system [37]. This equality reveals that the imaginary part of the response function can be directly measured from scattering experiments. This statement of the fluctuation-dissipation theorem is the central idea underpinning the extraction of dynamics from inelastic scattering data.

The relationship between real and imaginary parts of $\chi(\mathbf{q}, \omega)$ comes directly from their definitions. $\chi'(\mathbf{q}, \omega)$ can be rewritten as an integral over ω',

$$
\chi'(\mathbf{q}, \omega) = \int_{-\infty}^{\infty} d\omega' \sum_{i,f} \frac{e^{-\beta E_i}}{Z} |(\delta n_{\mathbf{q}})_{fi}|^2 \delta(\omega' - \omega_{fi})
$$

$$
\times \left\{ \mathcal{P}\left(\frac{1}{\omega - \omega'}\right) - \mathcal{P}\left(\frac{1}{\omega + \omega'}\right) \right\}
$$

$$
= \int_{-\infty}^{\infty} d\omega' S(\mathbf{q}, \omega') \left\{ \mathcal{P}\left(\frac{1}{\omega - \omega'}\right) - \mathcal{P}\left(\frac{1}{\omega + \omega'}\right) \right\} \quad (19)
$$

The two principal arguments can be evaluated in separate integrals:

$$
\chi'(q, \omega) = \int_{-\infty}^{\infty} d\omega' S(\mathbf{q}, \omega) \mathcal{P}\left(\frac{1}{\omega - \omega'}\right) - \int_{-\infty}^{\infty} d\omega' S(\mathbf{q}, \omega) \mathcal{P}\left(\frac{1}{\omega + \omega'}\right) \quad (20)
$$

Taking $\omega' \to -\omega'$ in the second integral and using Eq. (18),

$$
\chi'(\mathbf{q}, \omega) = -\frac{1}{\pi} \int_{-\infty}^{\infty} d\omega' \chi''(\mathbf{q}, \omega') \mathcal{P}\left(\frac{1}{\omega - \omega'}\right) \quad (21)
$$

This expression relating the real and imaginary parts of the complex-valued response function $\chi(\mathbf{q}, \omega)$ is an example of a Kramers–Kronig relation. A similar argument relates the imaginary part of χ to the real part by

$$
\chi''(\mathbf{q}, \omega) = \frac{1}{\pi} \int_{-\infty}^{\infty} d\omega' \chi'(\mathbf{q}, \omega') \mathcal{P}\left(\frac{1}{\omega - \omega'}\right) \quad (22)
$$

While the KK relations were derived here in terms of the density–density response function $S(\mathbf{q}, \omega)$, they are general for all causal response functions. A general derivation of the KK relations can be found elsewhere [36, 37, 44], but the derivation with respect to the measurable quantity $S(\mathbf{q}, \omega)$ is more relevant here.

The double differential scattering cross section of a photon scattering from a state $\mathbf{k}_i, \alpha_i$ to $\mathbf{k}_f, \alpha_f$ and from the system state $|i\rangle$ to $|f\rangle$ is derived from Fermi's golden rule [33]

$$
\frac{d^2\sigma}{d\Omega dE_f} = r_0^2 (\epsilon_{\alpha_i} \cdot \epsilon_{\alpha_f})^2 \left(\frac{E_i}{E_f}\right) \sum_i \sum_f |\langle f| \sum_j e^{i\mathbf{q}\cdot\mathbf{r_j}} |i\rangle|^2 \delta\left(\omega - (E_i - E_f)\right)
$$

$$
(23)
$$

where r_0 is the classical electron radius, ϵ_{α_i} and ϵ_{α_f} are polarization vectors, $\omega = \hbar\mathbf{k}_i - \hbar\mathbf{k}_f$, and $\mathbf{q} = \mathbf{k}_i - \mathbf{k}_f$. The sum over j is equal to the density operator $\delta n_{\mathbf{q}}$, and by renaming the matrix element $\langle f| \sum_j e^{i\mathbf{q}\cdot\mathbf{r_j}} |i\rangle = (\delta n_{\mathbf{q}})_{fi}$, the scattering

cross section is shown to be proportional to the dynamic structure factor $S(\mathbf{q}, \omega)$ [Eq. (8)]:

$$\frac{d^2\sigma}{d\Omega dE_f} = r_0^2(\epsilon_{\alpha_i} \cdot \epsilon_{\alpha_f})^2 \left(\frac{E_i}{E_f}\right) S(\mathbf{q}, \omega) \tag{24}$$

Equation (24) shows that to first-order, inelastic X-ray scattering measures the dynamic structure factor of electron density fluctuations in a system of charges. A measurement of $S(\mathbf{q}, \omega)$ can be used to recover the linear response function by directly applying the fluctuation-dissipation theorem and Kramers–Kronig relations.

In a system such as water, the form of the perturbation comes from the Coulomb potential of an external charge distribution,

$$\phi(\mathbf{q}, \omega) = \frac{4\pi e^2}{q^2} n_{\text{ext}}(\mathbf{q}, \omega) \tag{25}$$

where $n_{\text{ext}}(\mathbf{q}, \omega)$ is the time and space Fourier transformed external charge density. The electrodynamical linear response function is [31]

$$n_{\text{ind}}(\mathbf{q}, \omega) = \frac{4\pi e^2}{q^2} \chi(\mathbf{q}, \omega) n_{\text{ext}}(\mathbf{q}, \omega) \tag{26}$$

It follows from this that the recovered response function $\chi(\mathbf{q}, \omega)$ derived from $S(\mathbf{q}, \omega)$ and the Kramers–Kronig relation is related to the frequency- and wavevector-dependent dielectric constant $\epsilon(\mathbf{q}, \omega)$ [36]:

$$\frac{1}{\epsilon(\mathbf{q}, \omega)} = 1 + \frac{4\pi e^2}{q^2} \chi(\mathbf{q}, \omega). \tag{27}$$

In this case, $\chi(\mathbf{q}, \omega)$ propagates the charge induced in the system by an external charge distribution.

Our interest is the dynamics of molecular reorganization in liquid water. Energy scales relevant to these modes in liquids (meV) are much smaller than those relevant to plasmonic modes, particle–hole excitations, and ionization. Two assumptions are necessary to assert the equivalence of x-ray scattering measurements and molecular dynamics. First, the electron and nuclei wavefunctions are separable by the Born–Oppenheimer approximation. Second, the energy transfer is so small that it does not affect the electron wavefunction and therefore the electron density of a molecular scatterer. With these assumptions, the dynamical structure factor measured by inelastic X-ray scattering at meV energy transfers corresponds to fluctuations in the center of mass charge density in the system [33, 43].

C.   Experimental meV Inelastic X-Ray Scattering

The layout of a meV-resolution IXS instrument is shown in Fig. 4. While the specific construction of each meV IXS instrument is unique, they share the same general design. Each requires (1) a tunable meV-resolution monochromator, (2) spherical analyzer crystals that reflect particular X-ray energies with meV resolution, and (3) a long, rotatable arm to measure momentum transfer/scattering angle. In this section, we provide a basic description of these components, with particular examples drawn from the high-resolution inelastic X-ray scattering spectrometer at beamline ID-28 at the European Synchrotron Radiation Facility (ESRF) in Grenoble, France [45]. The data set presented in later sections was collected on this instrument. Also included is a discussion of the practical considerations for measuring and analyzing meV IXS data.

The energy of X-rays incident on the sample is defined by a tunable meV-resolution monochromator. The energy of synchrotron X-rays is typically $\sim$20 keV, with a typical energy bandwidth of 1 eV. To get 1 meV resolution (a 1000 $\times$ reduction), a highly selective monochromator system must filter most of the "white beam" intensity and transmit only a narrow band. This is done by scattering the beam off crystals with well-defined orientations and choosing a particular cross section of the scattered beam. A monochromator utilizes the fact that X-rays with
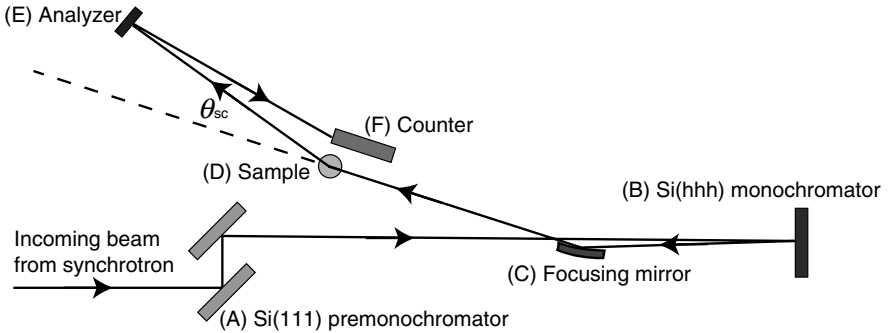
Figure 4.   A schematic drawing of a meV-resolution IXS beamline. The incoming beam is first incident on the premonochromator (**A**) to reduce the bandwidth of the beam to $\Delta E/E \sim 10^{-4}$. At the IXS beamline at ESRF, the premonochromator is comprised of a cryogenically cooled pair of Si crystals oriented to reflect the beam along their (111) Bragg reflections. Next the high-resolution monochromator (**B**) is positioned so that its (hhh) Bragg reflection backscatters the meV-resolution beam at an angle of 89.98°. A focusing mirror (**C**) routes the beam into the hutch. It focuses the beam to roughly (200 μm)^2 at the sample position (**D**). X-rays scattered by the sample at an angle of θ_{sc} are reflected by the analyzer (**E**) to the counter (**F**). The Bragg reflection of the analyzer is chosen to match the (hhh) reflection of the monochromator to match the energy resolutions. Details of the ESRF beamline can be found in Ref. [45] and references therein.

different energies scatter from the same Bragg reflection at different angles. For ID-28, 1 meV configuration has the premonochromaticized 21 keV beam scatter off the (11,11,11) reflection of a cryogenically cooled Si crystal ($\theta = 89.98°$) [45]. Because the scattering angle is so high, the configuration is referred to as a backscattering monochromator. This monochromator should also be tunable so that the incident energy can be chosen or scanned for an experiment. At ID-28, precise micro-Kelvin (μK) control of the monochromator temperature allows continuous control of the Si crystal's lattice constant through thermal expansion. This mechanism tunes the energy of X-rays selected from the chosen Bragg reflection, E_{mono}. To enable precise control of the crystal temperatures, the meV IXS monochromator comes after a coarser monochromator has already reduced the beam's energy spread. This decouples much of the heat load that comes from X-ray energy loss in the crystals from the high-resolution monochromator.

A spherical analyzer crystal is required to reflect scattered X-rays of a fixed energy to the X-ray detector. Typical meV IXS experiments measure over a particular energy transfer range (e.g., −50 to 50 meV). The analyzer is positioned to reflect X-rays of a fixed energy E_a to the counter, while the monochromator scans over the absolute energy range $E_{mono} = E_a - 50$ meV to $E_{mono} = E_a + 50$ meV. The energy transferred to the sample is simply $E_a - E_{mono}$. The analyzer is spherical to reflect all scattered X-rays to a focus at the detector. At ID-28, five analyzers positioned roughly 0.35 Å^{-1} apart in reciprocal space are constructed from small crystals glued to a curved substrate and matched to the Bragg reflection of the high-resolution monochromator [45]. The curved scattering geometry of the analyzer allows it to focus the incident X-rays with adequate precision to use multiple analyzers on the same spectrometer. The instrument at ID-28 measures IXS spectra with five analyzer/detector pairs at different q positions simultaneously.

The analyzer's q-position is determined by a rotating arm. The arm is typically very long to reduce the analyzer's angular acceptance of scattered X-rays. The arm length and maximum angle are determined by the construction of the beamline. The analyzers are fixed at the end of the arm, which rotates with the sample position at its center. For example, at ID-28, the 7 m arm rotates out to a maximum angle of 30°, which yields a maximum q-value of 6.0 Å^{-1} for X-ray energy ≈25 keV.

The intensity measured by an inelastic X-ray scattering experiment is proportional to the dynamical structure factor $S(q, \omega)$ broadened by the resolution profile of the instrument $R(\omega)$:

$$I(q, \omega) \propto \int_{-\infty}^{\infty} R(\omega - \omega')S(q, \omega')d\omega' \tag{28}$$

$R(\omega)$ is experimentally determined by measuring the energy spectra at the static structure factor maximum of a strongly scattering material such as plexiglass (PMMA). Examples of measured resolution functions from ID-28 at ESRF are
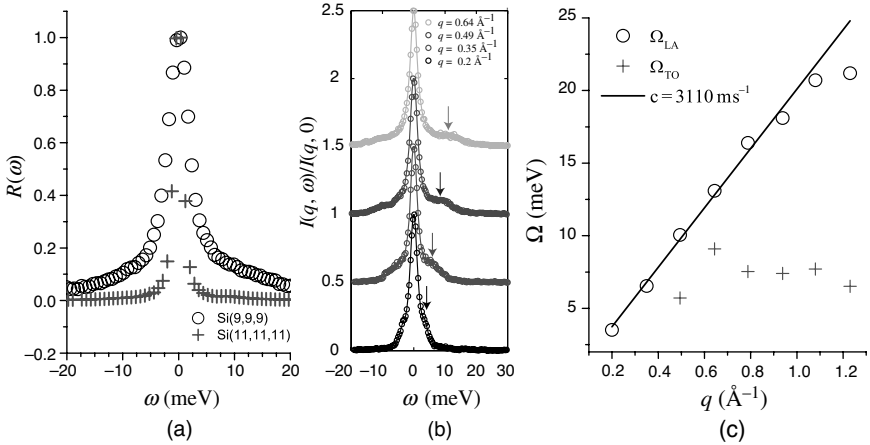
Figure 5. (**a**) Resolution functions for the Si(9,9,9) and Si(11,11,11) monochromator reflection on analyzer #2 of the IXS spectrometer at ID-28, ESRF (measured 09/2006). The resolutions of each are 4.0 and 1.8 meV, respectively, as defined by the FWHM of the resolution function profile. Each resolution function measurement is normalized to $E = 0$ meV value. (**b**) $I(q, \omega)$ measurements in room-temperature liquid water (open symbols) and the best-fit DHO model (solid lines) determined as described in the text. The arrows track the phonon-like sound mode in each spectra. These IXS spectra demonstrate collective modes in liquid water. The behavior of these features is quantified here to demonstrate consistency with other measurements. (**c**) After fitting all the low-q data, the dispersion relation for the modes in liquid water is found by plotting each mode's best-fit energy parameter $\Omega_i(q)$. The speed of sound of the high-speed longitudinal acoustic-like mode (LA) is 3100 ± 150 m s^{-1} (solid line), in agreement with previous measurements [30, 32]. The transverse optical-like mode (TO) appears only for $q > 0.4$ Å^{-1} and is slightly dispersive, as observed in other measurements [32, 78].

shown in Fig. 5a. Instrumental resolutions are typically cited as the FWHM of the measured resolution function. The q-resolution is determined by the solid angle subtended by the analyzer. It can be reduced by placing slits in front, with a corresponding reduction in intensity.

An example of a meV IXS spectra from room-temperature liquid water is provided in Fig. 5b. For length scales larger than the intermolecular distance, $S(q, \omega)$ has a general three-feature Brillouin line shape: a sharp quasielastic peak centered at $\omega = 0$ and the Stokes and anti-Stokes features representing dispersive density fluctuations. This line shape is characteristic of many condensed matter systems, with sharp phonon modes in crystals like ice [28, 46] and broad "phonon-like" modes in liquids [29, 30, 47], glasses [48, 49], and complex fluids [50–52].

Analyses of IXS measurements described in the previous section fit the measured intensity spectra to the convolution of the measured resolution function (or a Lorentzian fit) and a parameterized model of $S(q, \omega)$. For disordered systems such as liquid water, the spectra are fit with a Lorentzian peak to represent the

quasielastic scattering and damped harmonic oscillator (DHO) function for the dispersive modes. The form of the total line shape is [29, 45]

$$F(q, \omega) = I_0(q)\frac{\Gamma_0(q)^2}{\Gamma_0(q)^2 + \omega^2} + [n(\omega) + 1]\sum_i I_i(q)\frac{\omega\Gamma_i(q)^2\Omega_i(q)}{\left[\Omega_i(q)^2 - \omega^2\right]^2 + \Gamma_i(q)^2\omega^2}$$

(29)

where $n(\omega) = e^{-\beta\omega}/\left(1 - e^{-\beta\omega}\right)$ is the Bose factor. The sum over i generalizes the line shape to allow multiple dispersive features in $S(q, \omega)$ [30].

III.   GREEN'S FUNCTION IMAGING OF DYNAMICS WITH FEMTOSECOND TEMPORAL AND ANGSTROM SPATIAL RESOLUTION

As described in the introduction, IXS allows the spectrum of density fluctuations in water to be determined with high spatial and temporal resolution through measurements of the dynamical structure factor $S(q, \omega)$. We have also reviewed the theoretical approach to extracting the density response function from $S(q, \omega)$ through causality-enforcing Kramers–Kronig relations. The response function is a Green's function which allows the linear response reconstruction of hydration structures surrounding extended charge distributions [Eq. (25)]. This is a robust method for studying such experimentally infeasible systems.

In this section, we describe the procedure for reconstructing the dynamical response function $\chi(r, t)$ from a library of meV-resolution IXS measurements, leading to a new hybrid technique for studying molecular water and hydration dynamics. First, a complete measurement of $S(q, \omega)$ is made over a data range coextensive with the present limits of third-generation synchrotron X-ray sources. This enables the reconstruction of the density–density response function described in the previous section that tracks the average oxygen density correlations in water at high temporal and spatial resolution. The response function $\chi(q, \omega)$ is the direct measure of water response to an external point charge and is mathematically a Green's function. Combining this with linear response forms the basis of a new data-based perspective to solvation processes. Moreover, the Green's function can be used to reconstruct water dynamics around idealized dynamical charge distributions.

We then compare the extracted response function with state-of-the-art diffraction experiments, classical molecular dynamics (MD) simulations of diffusional relaxation, and femtosecond spectroscopic measurements. We then outline the procedure for combining the response function with image dynamical hydration structures. As a shorthand, we refer to this general approach as GFID. To illustrate the potential of GFID, we image the evolving hydration structure around an accelerating point charge moving near thermal velocity. Rather than the typical

abstraction of spherically symmetric hydration shells that rigidly follow a moving charge, these results indicate that charge movement strongly modifies the hydration structure, which evolves from a closed spherical shell to a cylindrical hydration "sleeve" with cylindrical symmetry. Finally, we discuss the strengths and weaknesses of GFID in the context of this "proof of concept" example.

A. Dynamical Response Function Extraction from meV IXS Measurements

The dynamic structure factor of water $S(q, \omega)$ was measured for energies to 80 meV over a q range from 0.2 to 7.2 Å^{-1}, as described elsewhere [53]. Most of the data were measured with incident X-ray energy of 21.747 keV ($\Delta E \approx 1.7$ meV for the Si(11,11,11) reflection). To improve counting statistics, data for $q > 6.0$ Å^{-1} were measured with the higher intensity Si(9,9,9) reflection with incident energy 17.794 keV ($\Delta E \approx 3.0$ meV). For large q, $S(q, \omega)$ has a broad shape, making this relatively small resolution difference insignificant. Example raw IXS spectra are shown in Fig. 6a. Corrections for sample holder scattering and different
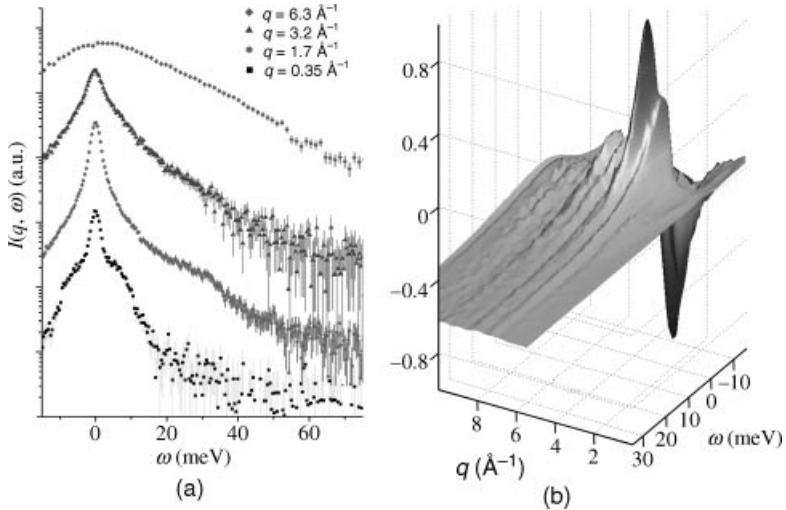
Figure 6. (a) Individual $S(q, \omega)$ scans from liquid water measured at beamline ID-28, European Synchrotron Radiation Facility. For $q \ll 2\pi/d$, where d is the average interparticle spacing, $S(q, \omega)$ has a characteristic Brillouin line shape: a quasielastic peak centered at $\omega \approx 0$ and the Stokes and anti-Stokes features indicating the collective modes of the system. For $q \gg 2\pi/d$, $S(q, \omega)$ appears as a Gaussian line shape (e.g., spectra $q = 6.3$ Å^{-1}) that is centered on higher energies for increasing q. For large values of q, $S(q, \omega)$ reflects the momentum distribution of particles in a liquid [79]. For room-temperature liquid water, $d = 2.8$ Å. (b) $\chi''(q, \omega)$ from applying the Bose factor $n(\omega)$ to the complete measurement of $S(q, \omega)$. While $\chi''(q, \omega)$ is shown to only $\omega = 30$ meV, it was measured to $\omega_{max} = 30$ meV to assure that all features contained in χ'' are captured in the data. Adapted from Ref. [53]. Copyright 2009 by the American Physical Society.

measurement efficiencies between analyzers were made to the raw measurements. The result is an experimental measurement of the complete dynamic structure factor of liquid water over the energy and momentum ranges relevant to molecular reorganization.

As described in detail in the previous section, the function $S(q, \omega)$ is a measure of the correlation of density fluctuations in a given medium [36]. It is related to the imaginary part of the linear response function $\chi(q, \omega) = \chi'(q, \omega) + \iota \chi''(q, \omega)$ by the fluctuation-dissipation theorem,

$$\chi''(q, \omega) = -\pi \left[S(q, \omega) - S(q, -\omega) \right] \tag{30}$$

A few technical considerations need to be accounted for before χ can be reconstructed from measurement.

IXS measurements with meV energy resolution have a low count rate due to the extreme reduction in intensity by the high-resolution monochromator. Experimentally, the compromise between measured energy range and counting statistics must be optimized to the objective of the measurement. As shown in the previous section, the detailed balance condition $S(q, -\omega) = e^{-\beta\omega} S(q, \omega)$ can be used to evaluate the energy loss from energy gain measurements. The counting statistics can be improved by measuring as little of the anti-Stokes part of each spectra as possible. For the measurement used in the following examples, the data were measured from -20 to $\sim$80 meV to observe the full quasielastic line. At $\omega = 80$ meV, the measured intensity is essentially at background levels. The quasielastic line is narrow in energy spread (width <1 meV) but has a high intensity. This feature is broadened by the instrumental resolution function, leading to an artificial contribution to the $S(q, \omega)$ measurements away from $\omega = 0$. Because of this, Lorentzian fits to the elastic line are subtracted from the data to remove artifacts. Finally, we evaluate Eq. (30) experimentally by dividing the $\omega > 0$ portion of $S(q, \omega)$ by the Bose factor $n(\omega) = (1 - e^{-\hbar\omega/kT})^{-1}$. Because the imaginary part of the response function is odd, we impose the condition $\chi''(q, -\omega) = -\chi''(q, \omega)$ on the $\omega > 0$ data (Fig. 6b).

We calculated $\chi'(q, \omega)$ from $\chi''(q, \omega)$ using KK relations, as previously described [53]. Fourier transforms require that the argument functions be defined on an infinite continuous domain. We extended the data onto a continuous interval using linear interpolation to avoid artifacts from finite, discrete data sets. The IXS data at the end points of the measurements in q and ω are essentially featureless and at background count levels. Moreover, extrapolation of the data beyond the maximum energy measured ω_{max} is also necessary because KK relations are defined as integrals from $-\infty$ to ∞. Numerical truncation of the integral at ω_{max} causes artificial oscillations in the transformation with period $2\pi/\omega_{max}$ to appear, influencing the characterization of any physical features. To avoid these artifacts, the data are extrapolated essentially to infinity in energy using the DHO model fit parameters described above. The form of the extrapolation affects density

fluctuations at much higher frequency than the temporal resolution of our measurement. The best-fit DHO model parameters were consistent with those reported in other IXS experiments on water. The known acoustic phonon mode with a sound velocity of 3100 ± 150 ms^{-1} is observed at low q values as expected (see Fig. 5 for comparison) [29, 30].

$S(q, \omega)$ data are measured by scanning the energy transfer ω at a fixed momentum transfer q. For each measured spectrum, the KK relation is applied to the measured and extrapolated χ'' to recover the real part $\chi'(q, \omega)$:

$$\chi'(q, \omega) = -\frac{1}{\pi} \int_{-\infty}^{\infty} d\omega' \chi''(q, \omega') \mathcal{P}\left(\frac{1}{\omega - \omega'}\right) \tag{31}$$

The full complex-valued $\chi(q, \omega)$ is then Fourier transformed,

$$\chi(q, t) = \int_{-\infty}^{\infty} \frac{d\omega}{2\pi} \chi(q, \omega) e^{-\iota\omega t} \tag{32}$$

to yield an intermediate function $\chi(q, t)$ that describes the temporal dynamics of the spatial Fourier components of the system response. Alternatively, $\chi(q, t)$ can be directly evaluated from $\chi''(q, \omega)$, without evaluating the real part. This is done by a sine transform as shown by Abbamonte et al. [54]:

$$\chi(q, t) = 2 \int_{-\infty}^{\infty} \frac{d\omega}{2\pi} \chi''(q, \omega) \sin(\omega t) \tag{33}$$

The KK method and the sine transform are mathematically equivalent.

The maximum scattering angle at third-generation beamlines limits the largest measurable momentum transfer. The spatial Fourier transform requires an extrapolation step to prevent density artifacts. The choice of extrapolation shape affects only density features that are much smaller than the interparticle spacing and therefore affects only length scales much smaller than the width of hydration shells. To extend the data, each profile for $\chi(q, t)$ was fit with a sufficient number (4 or 5) of Lorentzian peaks to capture its shape. The tails of this line shape were then used to enforce that $S(q, t) \to 0$ as $q \to \infty$, allowing the calculation of the Fourier transform integral. The spatial Fourier transform is spherical:

$$\chi(r, t) = \frac{1}{(2\pi)^2} \int_0^{\infty} q^2 dq \chi(q, t) \frac{2 \sin(qr)}{qr} \tag{34}$$

$\chi(r, t)$ is a Green's function that describes how a system responds to a δ-function perturbation at the origin at $t = 0$. Several frames of the reconstructed $\chi(r, t)$ are shown in Fig. 7a. $\chi(r, t)$ encapsulates the nonlocal charge density induced by a delta function charge perturbation at a distance r and time t from the origin. After the delta function impulse at $t = 0$, the water density relaxes in the form of "ripples"
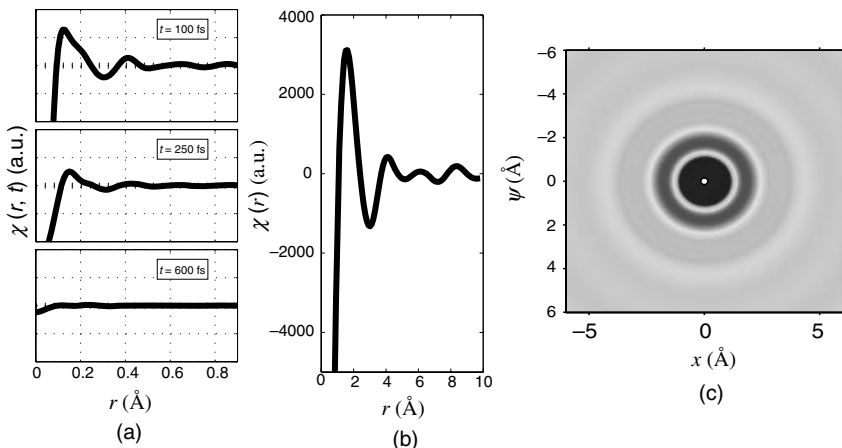
Figure 7. (**a**) The response function $\chi(r, t)$ at 100, 250, and 600 fs. At ~600 fs after the impulse, the hydration ripples have dissipated. (**b**) The hydration structure surrounding a point negative charge. The peak position at $r \approx 1.8$ Å indicates the position of the water oxygens in the first hydration shell. Since the ion is a point charge, no physical comparison exists to compare the position of the first hydration shell, but the distance between first and second hydration shells is comparable to the distance in bulk water from X-ray scattering measurements. The distance between first and second hydration shells around the point charge is 2.6 Å, which is almost exactly the distance in bulk water, $r_{\text{meas}} = 2.65$ Å [15]. (**c**) A 2D representation of the hydration structure around a point negative charge (white circle) at the origin. The dark ring centered 1.8 Å from the center represents an accumulation of oxygen density with respect to bulk. This color convention is used for the entire section. Adapted from Ref. [53]. Copyright 2009 by the American Physical Society.

representing the formation and dissipation of transient hydration shells around the origin. The amplitude of the density fluctuations is maximum after $t \sim 100$ fs and decays back to equilibrium bulk density. Residual density fluctuations are essentially indistinguishable from zero for $t \sim 1$ ps. Previous studies demonstrate a lack of an isotopic shift for D_2O relative to H_2O [29], which shows that $S(q, \omega)$ measured by IXS is dominated by motion of the center of mass of the entire water molecule [32]. The induced density is therefore the center of mass reorganization of the solvent eater in response to the perturbation.

The experimental energy and momentum resolutions place fundamental limits on the spatial and temporal range over observable phenomena in GFID. The energy sampling density of the measurement is much smaller than the energy resolution of the instrument ($\Delta E = 1.7$ meV). This limits the maximum time window to $2\pi/\Delta E = 2.8$ ps for the present measurement. This time window is much longer than the lifetime of any features in $\chi(r, t)$, as shown in Fig. 7a. In reciprocal space, the q-resolution of the instrument ($\Delta q = 0.03$ Å^{-1}) is smaller than the spacing

between measured q-transfers ($\sim 0.15\,\text{Å}^{-1}$), which limits the real space window to $2\pi/0.15\,\text{Å}^{-1} = 41\,\text{Å}$. These limits are far beyond all the structure and dynamics of interest on these scales and are therefore sufficient for capturing the entire usable water response.

The spatial and temporal resolutions of the Fourier transformed quantity $\chi(r, t)$ depend on the measured maximum momentum transfer q_{max} and energy transfer ω_{max}, respectively. An estimate of the resolution is the real space periodicity corresponding to the highest Fourier space value measured. For example, this measure of the spatial resolution Δr states that the smallest resolvable features in the quantity $\chi(r, t)$ will be spaced $\Delta r = 2\pi/q_{max}$ apart. However, the even ($\chi''(q, t) = \chi''(-q, t)$) and odd ($\chi''(q, \omega) = -\chi''(q, -\omega)$) properties of the response function provide information over a window twice the size of the measured one, and the resolution can be defined as twice that just using the highest frequency: $\Delta r = 2\pi/14.4\,\text{Å}^{-1} = 0.44\,\text{Å}$ and $\Delta t = (658\text{fs} \cdot \text{meV})2\pi/160\,\text{meV} = 26\,\text{fs}$ [54]. It has been shown that the center of mass dynamics of water to which IXS measurements are sensitive occur on much longer timescales [25]. Features in pair correlation functions for water representing intermolecular distances are much farther apart than the spatial resolution [14, 15].

B. Comparing $\chi(r, t)$ to Established Measurements

The density–density response function is a potentially powerful tool for investigating systems that are intractable for direct experimental techniques. It is necessary to verify that the features and timescales contained in the experimentally determined $\chi(q, \omega)$ reproduce existing results for simple systems. In this section, we describe direct comparisons between GFID and current state-of-the-art measurements from established methods.

Using GFID, we reconstruct the equilibrium ($t \sim \infty$) hydration structure surrounding an idealized negative point charge. This is given by the spherical Fourier transform of $\chi(q, \omega = 0)$ (Fig. 7b and c). Because IXS characterizes water's longitudinal response, the radial displacement of molecules can be observed. The generated hydration density shows the formation of defined hydration shells surrounding a point charge "ion." No true point charges exist in reality, so a direct comparison to a physical hydrated ion is impossible. The first hydration shell position indicates that it sits at the distance of closest approach for the finite-sized solvent molecule and an infinitesimal point charge. The distance between the first and second shells ($r = 2.6\,\text{Å}$) agrees well with the measured distance in bulk water ($2.65\,\text{Å}$) [15]. These results indicate that the hydration shells form at reasonable distances from the position of the point charge.

The diffusive relaxation dynamics of water can be reconstructed from this point charge ion example and compared to MD simulations. We use linear response

theory to calculate $\delta n_{\text{ind}}(\mathbf{q}, \omega)$, the charge density induced by an external time-dependent charge density $\delta n_{\text{ext}}(\mathbf{q}, \omega)$:

$$\delta n_{\text{ind}}(\mathbf{q}, \omega) = \frac{4\pi^2 e^2}{q^2} \chi(q, \omega) \delta n_{\text{ext}}(\mathbf{q}, \omega) \tag{35}$$

It is a measure of the time-dependent, ensemble-averaged oxygen density in water. We track the hydration structure relaxation for $t > 0$ after removing the point charge at $t = 0$ from its equilibrated hydration structure (Fig. 8a). We measure the time required by the system to lose memory of the point charge, relaxing back to bulk density. The density equilibration in the first hydration shell and at the origin is fit to exponentials with time constants of 125 and 113 fs, respectively. The density returns to its unperturbed value ($\delta \rho \approx 0$) after ~500 fs.

To assess the fidelity of the dynamics observed in GFID, we compare the relaxation of the point charge hydration structure with MD simulations using SPC/E water. We average the density response from over 1000 MD simulation trajectories from ion-water systems in which an ion is removed at $t = 0$ from an equilibrated system (Fig. 8b, inset) [53]. The MD hydration structures initially show typical water packing around an ion with well-developed solvation peaks. After the ion is removed, the profile relaxes to bulk density as water molecules diffuse to fill the void, leading to a decay of the profile and filling of the ion cavity. The relaxation of the first hydration shell to the bulk value depends on the ion size and charge. In all cases, it is roughly exponential with a time constant between 60 and 90fs. This is slightly faster than the found from GFID. This slight difference is not surprising, given that the SPC/E water model overestimates the water diffusion constant [55]. Owing to the asymmetric charge structure of the water molecule, and correspondingly of the hydration structures for positively and negatively charged solutes, there exists a real physical difference in the relaxation dynamics for cations and anions. These results point out a limitation of GFID in its simplest implementation, which is that an implementation of excluded volume for water hydrating finite-sized structures is missing. We return to this point in the next section. Furthermore, GFID intrinsically does not account for the cation/anion hydration asymmetry. In linear response, hydration structures differ only by their sign surrounding positive or negative charges. In spite of these limitations of linear response and of classical molecular dynamics, the similar results indicate that the basic physics of hydration are captured in GFID.

These meV-IXS experiments are particularly sensitive to oxygen dynamics in water. Underdamped density oscillations can be observed for length scales larger than 3 Å($q < 2$ Å^{-1}) in the intermediate response function $\chi(q, t)$ (Fig. 8b). 3 Å is roughly the distance between two O atoms in water. In this q-range, the oscillations have a period that varies between 180 and 250 fs, with the period having an
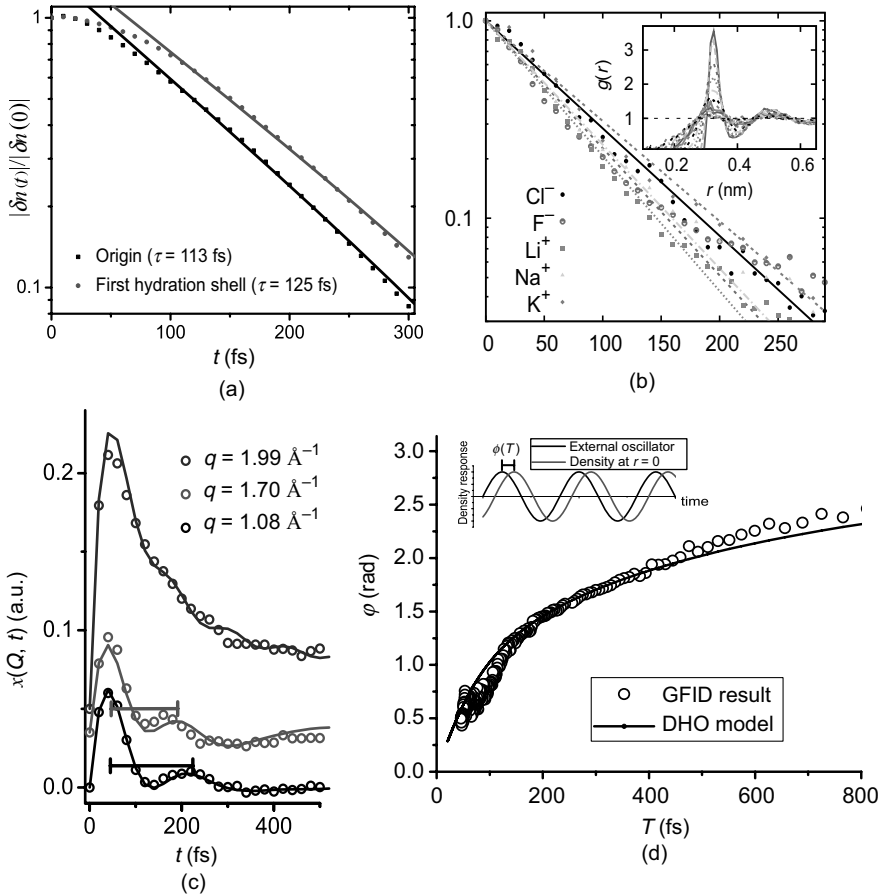
Figure 8. Diffusional relaxation of water structure in response to the removal of an ion is compared to MD simulations using SPC/E water. (**a**) After ion removal, the GFID reconstructed density returns to the bulk value at the origin (black) and in the first hydration shell (gray) exponentially with time constants $\tau = 113$ and 125 fs (solid lines, fit for $t > 50$ fs), respectively. (**b**) Normalized first peak height $g_{max}(t)$, shown as $\Delta g(t)/\Delta g(0) = (g_{max}(t) - 1)/(g_{max}(0) - 1)$, is obtained for five ion types; (inset) MD radial distribution function $g(r, t)$ of water oxygens: 15 different profiles are shown for $t = 0, 20, 40, \ldots, 280$ fs. Fit exponential time constants vary from 64 fs (for Li^+) to 86 fs (for K^+). (**c**) $\chi(q, t)$ from IXS data (open symbols) show underdamped density oscillations for intermolecular distances ($q < 2$ Å^{-1}), but not for intramolecular distances ($q > 2$ Å^{-1}). For each q-value, the corresponding curve from the best-fit DHO model is shown. The temporal period of this mode varies between 250 fs (black bar) and 180 fs (gray bar) at 1.08 Å$^{-1} < q < 1.7$ Å^{-1}, consistent with an O–O oscillation. (**d**) For a sinusoidal driving frequency of an amplitude monopole, the steady-state induced density lags by phase $\phi(T)$. For $T \gg 200$ fs, $\phi(T)$ can be approximated by the phase lag of a damped, driven harmonic oscillator (solid line). For $T \ll 200$ fs, the behavior deviates strongly from the harmonic oscillator. Adapted from Ref. [53]. Copyright 2009 by the American Physical Society.

inverse relationship with q (Fig. 8c). Inversions of the best-fit DHO functions are plotted to show that the origins of these oscillations are the dispersive modes of the dynamic structure factor. For the smallest length scales that exhibit this oscillation (corresponding to 3 Å), the density oscillation has a period of $\sim$200 fs. For larger q values corresponding to intramolecular distances, this oscillation mode vanishes, which is expected for an intermolecular O–O feature. The limiting 3 Å period is close to the measured 170 fs period of ($q = 0$) O–O oscillation between water molecules from femtosecond IR absorption spectroscopy [24], which is used to measure the oscillatory dynamics in liquid water.

A standing wave point charge source can be used to probe the oscillatory dynamics of the response function in more detail. We reconstruct the behavior of water in the presence of a THz frequency charge monopole at the origin using $\delta n_{\text{ext}}(\mathbf{r}, t) = \delta(\mathbf{r}) \sin(2\pi t/T)$. The temporal and spatial Fourier transform of this source is simply the sum of delta functions, $\delta n(q, \omega) = \delta(\omega - 2\pi/T) - \delta(\omega + 2\pi/T)$. With this representation, the steady-state hydration dynamics are simply the spherical Fourier transform of $\chi(q, \omega = 2\pi/T) - \chi(q, \omega = -2\pi/T)$. The GFID response of the solvent structure is sinusoidal with the same period as the driving monopole but lags it by a frequency-dependent phase shift, $\phi(\omega) = \tan^{-1}(\chi''(\omega)/\chi'(\omega))$ (Fig. 8d, inset). For comparison, we fit the measured phase shift to that of a driven harmonic oscillator in a damping viscous fluid, for which the analytical phase shift is $\tan \phi(\omega) = \omega\gamma/(\omega_0^2 - \omega^2)$, where ω_0 is the resonant frequency and γ is the viscous damping parameter of the fluid [37]. Clearly, the harmonic oscillator model does not fit the behavior of water over the full range of periods. For high driving frequencies ($T < 100$ fs), the water response at the origin lags behind the oscillator by a smaller than expected phase shift. As the driving period increases (100 fs $< T < 200$ fs), this phase shift increases drastically. Limited agreement with driven harmonic oscillator models is observed for $T \gg 200$ fs (Fig. 8d). The fit resonant frequency ω_0 of 17.2 meV implies a temporal period of 240 fs, consistent with the reconstructed range of values for O–O oscillation from the intermediate function $\chi(q, t)$ for this q range.

For rapid oscillations ($T < 120$ fs), the GFID phase shift deviates from the analytic model, indicating a different regime of response. The slope in the phase shift $\phi(\omega)$ flattens out for small T (Fig. 8d). The Green's function cannot respond to the rapidly changing external charge distribution. The crossover is indicative of how quickly center of mass reorganization occurs in water. From simulation and spectroscopic experiments, it is observed that water has two modes of molecular response: a fast mode from inertial motions with characteristic timescales of tens of femtoseconds and a slow mode due to diffusional motion on the scale of hundreds of femtoseconds [25]. Although it does not prove the existence of two modes, the behavior of the phase shifts near a standing wave source is consistent with this picture.

C.   An Example of GFID Reconstructed Movies: The Evolution of Hydration Around an Accelerating Point Charge

The dynamics of the solvent surrounding an external charge density can be reconstructed from IXS data by directly applying the linear response relation defined in Eq. (35). As an example, GFID is used to examine inertial effects by monitoring the evolving hydration structure around an idealized point charge ion accelerating harmonically in a THz field ($v(t) = v_0 \sin(\omega t)$, $v_0 = 500 \, \mathrm{m \, s}^{-1}$, $\omega = 2\pi/2 \, \mathrm{ps}$) (Fig. 9). The red isosurfaces represent the hydration structure, defined as regions of enhanced water oxygen density induced by the external charge distribution. Three frames of the first 600 fs show the evolution of the hydration shell as the point charge accelerates from 0 to v_0. The hydration shell is initially spherical, but is progressively replaced by a hydration sleeve of cylindrical symmetry. The spherical shell weakens and the leading edge thins within the first 100 fs of linear motion. As v increases to its maximum, the point charge breaks through the first hydration shell, which exhibits significant longitudinal distortion along the axis of movement. This indicates an asymmetric radial reorganization of oxygen density. At $\sim$500 fs, the hydration structures form a steady-state cylindrical hydration sleeve, followed by a trail of reduced oxygen density with a velocity-dependent length. This shows that the hydration structures near moving solutes are different from those for stationary solutes. Also, due to the influence of the hydration structure on chemical reactions, moving reactants might participate very differently from stationary ones.

In the implementation described in this section, GFID calculates the response of a continuous, dynamical dielectric to an embedded charge density. While this linear response formalism is rigorous, it is missing a description of excluded volume required to apply the GFID technique to extended objects such as ions and molecules. The Pauli exclusion principle prevents molecules from "overlapping," requiring an extended molecule or surface to have an impenetrable volume.

Figure 9. (a–c) The evolution of hydration structure around a point charge (white sphere) as it accelerates harmonically to $v_0 = 500 \, \mathrm{m \, s}^{-1}$ in 500 fs. 3D renderings were generated using the software package VMD [80]. Adapted from Ref. [53]. Copyright 2009 by the American Physical Society.

(a) $t = 200$ fs   (b) $t = 400$ fs   (c) $t = 600$ fs
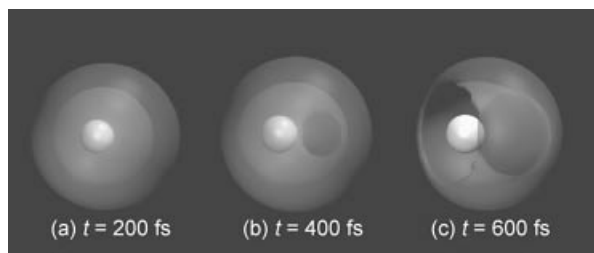
The size of this volume determines many of the solvation properties of the molecule. Examples are the increase in solvent hydrogen bonding [56] and hydrogen bond reorientation lifetimes [57] around monovalent anions as the ionic size increases. The excluded volume of a solute is an important part of the electrodynamical description of molecular hydration. A complete GFID approach for studying hydration around solutes needs a method that takes into account the expulsion of solvent from a cavity representing a solute's excluded volume.

IV. AN EXCLUDED VOLUME IMPLEMENTATION FOR GREEN'S FUNCTION IMAGING OF DYNAMICS

The linear response function $\chi(\mathbf{q}, \omega)$ is defined to propagate the solvent reorganization effect of an external charge density. In the presence of a dynamical charge density $\delta n_{\text{ext}}(\mathbf{q}, \omega)$, the induced charge $\delta n_{\text{ind}}(\mathbf{q}, \omega)$ is

$$\delta n_{\text{ind}}(\mathbf{q}, \omega) = \frac{4\pi^2 e^2}{q^2} \chi(q, \omega) \delta n_{\text{ext}}(\mathbf{q}, \omega) \tag{36}$$

To this point, we have demonstrated a technique to extract the linear response function from a library of meV IXS spectra corresponding to the femtosecond-scale density fluctuations in water. As a proof of concept, the resulting $\chi(q, \omega)$ was applied to simple dynamical charge systems such as slowly accelerating point charges, for which Eq. (36) is correct. However, this formalism becomes unphysical when trying to describe the response to *extended* charge densities such as ions, molecules, and interfaces. Equation (36) describes the response of a continuous medium to embedded charge distributions, permitting the solute and solvent charge distributions to occupy the same volume. Physical, charged systems such as ions and molecules are prevented from overlapping their volume with solvent molecules due to the Pauli exclusion principle. This linear response formalism requires a way to describe excluded volume before it can effectively describe the solvation structure surrounding realistic charge distributions.

In this section, we describe how GFID can be generalized from abstract, point charge systems to molecular ones. First, we show that a direct application of linear response theory fails to accurately describe the hydration environment around physical, finite-sized molecular solutes. Next, an implementation of solute excluded volume is introduced. Using a combination of linear response and excluded volume, we use GFID to generate hydration structures for static and dynamical "molecules" and show that they are consistent with those of well-studied molecular systems. This provides us with a toolkit to reconstruct hydration dynamics around molecular systems using the full Green's function.

A.   Green's Function Imaging of Dynamics with Excluded Volume

$S(\mathbf{q}, \omega)$ is a measure of electron density fluctuations in a bulk material [36]. The related response function $\chi(\mathbf{q}, \omega)$ is related to the inverse of the dielectric function $\epsilon(\mathbf{q}, \omega)$,

$$\frac{1}{\epsilon(\mathbf{q}, \omega)} - 1 = \frac{4\pi e^2}{q^2} \chi(\mathbf{q}, \omega) = \mathcal{L}(\mathbf{q}, \omega) \tag{37}$$

The quantity $\mathcal{L}$ is known as the dielectric loss function. In the limit of the previously outlined assumptions, the density response function is a Green's function that can be used to image the dynamical hydration structure around a defined external charge density. The Fourier space linear response relation between the induced charge density $\delta n_{\mathrm{ind}}(\mathbf{q}, \omega)$ and the external charge density $\delta n_{\mathrm{ext}}(\mathbf{q}, \omega)$ is

$$\delta n_{\mathrm{ind}}(\mathbf{q}, \omega) = \mathcal{L}(q, \omega)\delta n_{\mathrm{ext}}(\mathbf{q}, \omega) \tag{38}$$

which is a simplification only in terminology from the previous definition. $\mathcal{L}(q, \omega)$ and its Fourier transform $\mathcal{L}(r, t)$ will be used in this discussion rather than the raw response function to keep the mathematics uncluttered. Reviews of the relationship between the density–density response function $\chi(\mathbf{q}, \omega)$ and the dielectric function $\epsilon(\mathbf{q}, \omega)$ can be found in the following references [33, 36].

Using the linear response relation [Eq. (38)] and a measurement of $\chi(\mathbf{q}, \omega)$, the induced charge density in a polarizable medium $\delta n_{\mathrm{ind}}(\mathbf{q}, \omega)$ can be determined for an external charge density $\delta n_{\mathrm{ext}}(\mathbf{q}, \omega)$. This formulation of linear response is useful for point charge assemblies, but it fails in the case of physical, finite-sized charge densities representing physical solutes, such as ions and molecules [58].

The induced charge density is related to the convolution of the real space loss function $\mathcal{L}(r, t)$ and the external charge distribution $\delta n_{\mathrm{ext}}(\mathbf{r}, t)$. For a $\delta n_{\mathrm{ext}}(\mathbf{r}, t)$ of finite extent, contributions to the induced charge density from different parts of $\delta n_{\mathrm{ext}}(\mathbf{r}, t)$ can cancel due to destructive interference, because $\mathcal{L}(r, t)$ describes both induced positive and negative densities. Physically, the external charge density becomes too large for water molecules to organize hydration shells around it, and the granularity described by $\mathcal{L}(r, t)$ becomes washed out. Equation (38) describes an external charge distribution embedded in a continuous dielectric that induces a bound charge density in response to an external potential. This formalism fails to accurately describe the solvation charge response due to a molecular solute in liquid water. Solutes are defined by their charge distribution and by an excluding volume in which liquid water itself is forbidden from penetrating. The physical basis for this is the Pauli exclusion principle, where overlapping electron wavefunctions are forbidden. To use GFID for molecules, it is important to include a description of the excluded volume of the solute charge distribution in the hydration structure. What is needed is schematically represented in Fig. 10.
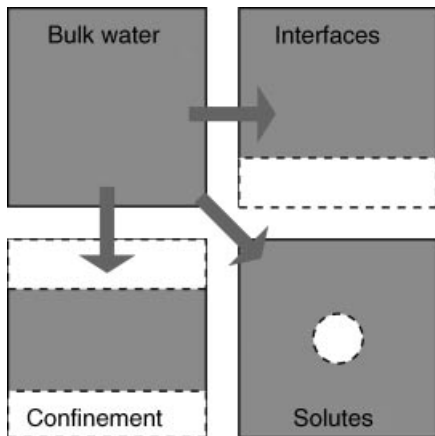
Figure 10. The bulk Green's function is extracted from IXS data. To treat problems such as water near solid surfaces, water surrounding solutes, and confined water, we need to remove the contributions from the volumes schematically shown in the diagram.

B. Linear Response Formalism with Excluded Volume

A solution to a similar excluded volume problem is required in quantum chemistry when seeking the electronic structure and excitation energies of dissolved molecules. Simulations involving explicit solvent molecules rapidly become computationally expensive as the size of the simulation volume increases. Implicit solvent models where the solvent is modeled as an infinite dielectric can be utilized to describe the hydration environment more efficiently, but they lack molecular details. More complicated models account for the dynamical or nonlocal solvent behavior derived from simulations or analytical approximations [59]. The solute is modeled as an assembly of nuclear charges, a functional basis representing electron density, and a cavity chosen to reflect the solute's morphology. For example, a simple molecular cavity can be the volume bounded by a set of spheres, centered on each atom in the molecule with the respective radii matching one that is empirically determined (e.g., the van der Waals radius). For the case of GFID, combining the dielectric loss function formalism in Eq. (38) with a similar implementation of excluded volume is an apt method for describing physical solutes.

The interior of an excluded volume is by definition devoid of solvent and unpolarizable ($\epsilon = 1$), and the surrounding solvent behaves as bulk solvent. The dielectric loss function can be modified to enforce the boundary:

$$\mathcal{L}^{\mathrm{mod}}(|\mathbf{r} - \mathbf{r}'|; \omega) = \begin{cases} 0, & \mathbf{r} \text{ or } \mathbf{r}' \in V_{\mathrm{exc}} \\ \mathcal{L}(|\mathbf{r} - \mathbf{r}'|; \omega), & \mathbf{r} \text{ and } \mathbf{r}' \notin V_{\mathrm{exc}} \end{cases} \tag{39}$$

where $\mathcal{L}$ is determined from IXS measurements of $\chi(r, t)$ as described in Eq. (37). The boundary conditions on the dielectric function ϵ are accordingly:

$$\epsilon^{\mathrm{mod}}(|\mathbf{r} - \mathbf{r}'|; \omega) = \begin{cases} 1, & \mathbf{r} \text{ or } \mathbf{r}' \in V_{\mathrm{exc}} \\ \epsilon(|\mathbf{r} - \mathbf{r}'|; \omega), & \mathbf{r} \text{ and } \mathbf{r}' \notin V_{\mathrm{exc}} \end{cases} \tag{40}$$

ϵ has the vacuum value of 1 inside the solute's excluded volume. For isotropic systems such as liquid water, $\mathcal{L}$ depends only on the distance between the points $\mathbf{r}$ and $\mathbf{r}'$. In general, it is a two-point function: the effect of electrodynamical quantities at a point in space $\mathbf{r}'$ is propagated to the point $\mathbf{r}$. This can be seen in the real space equivalent of Eq. (38):

$$n_{\text{ind}}(\mathbf{r}; \omega) = \int_{-\infty}^{\infty} d\mathbf{r}' \mathcal{L}(\mathbf{r}, \mathbf{r}'; \omega) n_{\text{ext}}(\mathbf{r}'; \omega) \qquad (41)$$

Relating the external charge density to the induced one is a problem for this definition of $\mathcal{L}^{\text{mod}}$. Equation (38) propagates the influence of the charge density at the point $\mathbf{r}'$ to the position $\mathbf{r}$, but the boundary conditions as defined cancel any charge density induction if the external charge distribution is completely contained within the excluded volume. $\mathcal{L}^{\text{mod}}$ is nonzero only where n_{ext} is zero, making their product uniformly zero. Eq. (38) and the modified loss function $\mathcal{L}^{\text{mod}}$ are incompatible because the localized external charge densities do not contribute to charge induction in the media by definition.

Previous work on solute–solvent interactions suggest that the nonlocal fields generated by localized charges can be used, rather than the charges themselves [60–63]. The electric displacement $\mathbf{D}(\mathbf{r})$ is a property of the localized external charge distribution that spans all space. $\mathbf{D}(\mathbf{r})$ from the solute induces a polarization at all points in the solvent:

$$P_\alpha(\mathbf{q}, \omega) = -\left(\epsilon_{\alpha\beta}^{-1}(\mathbf{q}, \omega) - 1\right) D_\beta(\mathbf{q}, \omega) = -\mathcal{L}(\mathbf{q}, \omega) D_\beta(\mathbf{q}, \omega) \qquad (42)$$

where $\epsilon_{\alpha\beta}^{-1}$ is the inverse dielectric tensor. $\epsilon_{\alpha\beta}^{-1}$ and $\mathcal{L}_{\alpha\beta}$ are tensorial forms of ϵ^{-1} and $\mathcal{L}$ found in Eq. (37) [36]. $\mathcal{L}_{\alpha\beta}$ can be written explicitly in terms of its longitudinal and transverse components [64]:

$$\mathcal{L}_{\alpha\beta}(\mathbf{q}, \omega) = \mathcal{L}(q, \omega)\frac{q_\alpha q_\beta}{q^2} + \mathcal{L}_\perp(q, \omega)\left(\delta_{\alpha\beta} - \frac{q_\alpha q_\beta}{q^2}\right) \qquad (43)$$

The longitudinal component $\mathcal{L}(q, \omega)$ is derived from IXS measurements. The transverse component $\mathcal{L}_\perp(q, \omega)$ is important in magnetic systems and when studying intramolecular charge reorganization like rotation [64]. The characteristic timescale for oxygen oscillation in water is $\sim$200 fs [24, 53], so the molecular dynamics of interest in water occur on timescales of hundreds of femtoseconds. The inertial reorganization of water molecules occurs on the order of tens of femtoseconds, so the transverse component can be ignored when the relative motions of water molecules are of interest. The dynamical polarization induced in the solvent surrounding a solute molecule is related to the solute's dynamical electric displacement $\mathbf{D}(\mathbf{q}, \omega)$ and the Fourier transform of the modified dielectric

loss tensor, $\mathcal{L}^{\text{mod}}_{\alpha\beta}(\mathbf{q}, \omega)$ in linear response,

$$P_\alpha(\mathbf{q}, \omega) = \mathcal{L}^{\text{mod}}_{\alpha\beta}(\mathbf{q}, \omega)D_\beta(q, \omega) \tag{44}$$

with an implicit sum over β. The relationship between the electric displacement and the induced polarization is defined in Fourier space for simplicity, but it is also helpful to calculate these quantities in real space. Equation (44) is a convolution in real space:

$$P_\alpha(\mathbf{r}, t) = \int_{-\infty}^{t} dt' \int_{-\infty}^{\infty} d\mathbf{r}' \mathcal{L}^{\text{mod}}_{\alpha\beta}(|\mathbf{r} - \mathbf{r}'|; t - t')D_\beta(\mathbf{r}'; t') \tag{45}$$

where $\mathcal{L}^{\text{mod}}_{\alpha\beta}(|\mathbf{r} - \mathbf{r}'|; t - t')$ is the Fourier transform of the tensor $\mathcal{L}^{\text{mod}}_{\alpha\beta}(\mathbf{q}, \omega)$ that integrates the modified density response function [Eq. (39)] into the polarization calculation. The goal for this procedure to image the hydration structure surrounding a defined dynamical molecular solute, as indicated by the induced charge density. It can be computed directly from the real space polarization,

$$n_{\text{ind}}(\mathbf{r}, t) = -\nabla \cdot \mathbf{P(r, t)} \tag{46}$$

$P_\alpha(\mathbf{r}, t)$ is uniformly zero for $\mathbf{r} \in V_{\text{exc}}$ as defined in Eq. (39), which is consistent with our definition of excluded volume. Solvent that would mediate charge induction is forbidden from the inside the cavity. For $\mathbf{r} \notin V_{\text{exc}}$, $P_\alpha(\mathbf{r}, t)$ is dependent on the displacement field over all space *except* from the cavity. Equation (45) can be written in terms of the boundary-free induced polarization $P^0_\alpha(\mathbf{r}; t)$ and a boundary-enforcing correction $\delta P_\alpha(\mathbf{r}; t)$:

$$P_\alpha(\mathbf{r}; t) = \begin{cases} 0, & \mathbf{r} \in V_{\text{exc}} \\ P^0_\alpha(\mathbf{r}; t) - \delta P_\alpha(\mathbf{r}; t), & \mathbf{r} \notin V_{\text{exc}} \end{cases} \tag{47}$$

where

$$P^0_\alpha(\mathbf{r}; t) = \int_{-\infty}^{t} dt' \int_{-\infty}^{\infty} d\mathbf{r}' \mathcal{L}_{\alpha\beta}(|\mathbf{r} - \mathbf{r}'|; t - t')D_\beta(\mathbf{r}'; t') \tag{48}$$

and

$$\delta P_\alpha(\mathbf{r}; t) = \int_{-\infty}^{t} dt' \int_{V_{\text{exc}}} d\mathbf{r}' \mathcal{L}_{\alpha\beta}(|\mathbf{r} - \mathbf{r}'|; t - t')D_\beta(\mathbf{r}'; t') \tag{49}$$

The correction discards the nonlocal contribution to the induced polarization from the cavity V_{exc} at all points. For $\mathbf{r} \in V_{\text{exc}}$, $P_\alpha(\mathbf{r}; t) = 0$, which accounts for the lack of polarizable solvent inside the cavity. Equation (47) is an equivalent approach to the one defined by Eq. (45).

It is notable that this general approach for describing the excluded volume has been used in other systems. For example, it has been used to describe model solute–solvent systems where the solvent is approximated as a continuous dielectric [60–63]. These boundary conditions have been shown to underestimate the long-time relaxation that is better captured in more accurate treatments, such as Gaussian field models of solvation. In these, an inverse tensor of the dielectric loss function is used rather than a simple subtraction of the cavity contribution [65]. In principle, it is possible to compare the Gaussian solvation model and the cavity subtraction approach with our data. However, the timescales over which a difference is observed [65] is significantly longer than the longitudinal relaxation lifetime of water ($\sim$0.7 ps) [22]. In the case of our measurements, the extracted response function has largely decayed to low signal levels over this timescale. The observable difference between the two theoretical formalisms is likely on the scale of other sources of noise in the measurement.

A benefit of this implementation over the tensorial approach is computational efficiency. Tensor inversion can be implemented within GFID, but becomes computationally expensive when imaging dynamical solvation structures due to the added computation of inverting the two-point susceptibility tensor over all points in space at each time step. By comparison, the spatial parts of Eqs. (48) and (49) can be calculated using fast Fourier transform (FFT) at each time step and are computationally efficient. Equation (49) is written as an integral over the excluded volume, which is incompatible with FFTs. However, introducing a "filter" function $\Theta(\mathbf{r}; V_{\text{exc}}) = \sum_{\mathbf{r}_i \in V_{\text{exc}}} \delta(\mathbf{r} - \mathbf{r}_i)$ allows it to be written as an integral over all space and therefore capable of being evaluated with an FFT:

$$\delta P_\alpha(\mathbf{r}; t) = \int_{-\infty}^{t} dt' \int_{-\infty}^{\infty} d\mathbf{r}' \mathcal{L}_{\alpha\beta}(|\mathbf{r} - \mathbf{r}'|; t - t') D_\beta(\mathbf{r}'; t') \Theta(\mathbf{r}'; V_{\text{exc}}) \quad (50)$$

C. Examples

Using this form of GFID, it is possible to reconstruct the hydration structure around an external charge density with explicit excluded volume. In the following examples, the density response function for liquid water used is from the measurements described in the previous section.

1. Static Hydration Structure Around Ions

The simplest model of a classical ion is a charge distribution centered inside with a spherical excluded volume. The difference in excluded volume from which solvent water molecules are prohibited is one of the most important differences between ionic species of the same charge. In many classical molecular dynamic models of water, a simulated ion is implemented as a charge contained in a Lennard-
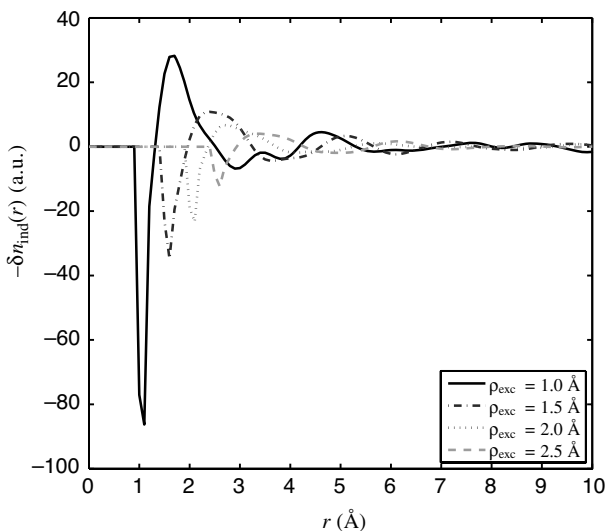
Figure 11. For a fixed external charge distribution (a Gaussian with width $\sigma_Q = 0.3$ Å), the excluded volume radius r_{exc} is varied from 1.0 to 2.5 Å. The induced charge density $\delta n_{ind}(r)$ is plotted as a function of the distance from the center of the external charge distribution. The position of the first minimum (negative induced charge density) represents the first hydration shell position of oxygen, as it carries the negative charge density in water. This peak position can be continuously controlled by the parameter r_{exc}. Adapted from Ref. [58].

Jones sphere with a diameter that varies with species. Using GFID and excluded volume, we can examine the effect of the charge distribution size and diameter independently and compare the results with measurements.

First, we investigate the induced charge density in the surrounding medium as a function of cavity size (Fig. 11). The position of the induced negative charge density, and therefore the water oxygen atoms, represents the position of solute's hydration shells. For this example, the excluded volume is a sphere of radius r_{exc}. We can adjust the position of the first hydration shell to match the values determined by other methods for the desired ionic species by the choice of r_{exc}. The effect of spatial distribution of charge can be independently controlled for fixed excluded volume. Figure 12 shows how the magnitude and the shape of the induced charge density is affected by the spatial distribution of charge for a fixed cavity radius ($r_{exc} = 2$ Å). The induced negative charge density around the excluded volume decreases in magnitude as the external charge distribution leaks into the medium. For a particular coordinate $\mathbf{r}$, less charge is contained within the sphere of radius $|\mathbf{r}|$. As expected from Gauss's law, the displacement vector $\mathbf{D}(\mathbf{r})$ and the induced polarization $\mathbf{P}(\mathbf{r})$ are weakened.
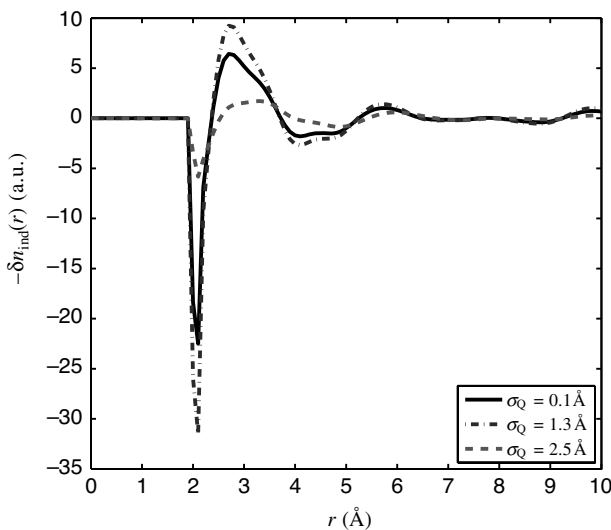
Figure 12. The effect of the diameter of the charge for a fixed excluded volume ($r_{exc} = 2$ Å). The external charge distributions are modeled as Gaussians centered at the origin with widths $\sigma_Q = 0.1$ Å (induced charge density shown as a solid line), $\sigma_Q = 1.3$ Å (dash-dot line), and $\sigma_Q = 2.5$ Å (dotted line). When the charge is mostly contained within the excluded volume, the induced charge density is nearly conserved ($\sigma_Q = 0.1, 1.3$ Å). For larger distributions ($\sigma_Q = 2.5$ Å), where significant fractions of charge penetrate the surrounding medium, the induced charge density is weakened. Additionally, the induced features are slightly broadened compared to the narrower charge distributions. Adapted from Ref. [58].

We can adjust these parameters to match calculated hydration structures with known ions. Anions such as Cl^- and F^- have well quantified first-coordination shell ion–oxygen positions of $\sim$3.1 Å [66] and $\sim$2.7 Å [67, 68], respectively. Using the excluded volume radius r_{exc} and charge width σ_Q as tunable parameters, a library of hydration structures can be generated. The electron density for each ion is calculated using GAMESS, a density functional theory software package [69]. Using these calculated charge distributions, we find good agreement in the first peak position of negative induced charge density and the known ion–oxygen distance when r_{exc} is $\sim$2.25 Å for Cl^- and $\sim$1.75 Å for F^-. These values for r_{exc} are larger than the bare ion radii (1.81 Å for Cl^-, 1.36 Å for F^-) [70]. This is not surprising due to the solvent water molecule's own finite size. The approach of "tuning" the excluded volume according to known hydration structures could help determine physical excluded volume parameters for similar systems that have unknown solvation structure. An example of this is using the known methane hydration structure from simulation [71] to find the effective excluded volume in GFID for

a C–H group. These parameters can then be used to estimate the excluded volume of C–H groups in more complicated organic molecules such as hydrocarbons.

2. Dynamical Hydration Structure Around Dynamical Charge Distribution: Coumarin Photoexcitation

Charge density changes from solute electronic excitations are simple systems to study dynamical hydration structure changes. Coumarins are a class of organic chromophores used as a gain medium in dye lasers [72]. They have also been used to study solvation dynamics experimentally [25] and theoretically [73]. Here, we use a model of the ground state and excited state charge density of a coumarin anion as a GFID input to observe the hydration structure dynamics around a dynamical model solute.

The molecular structure and excluded volume of a coumarin ion (C343$^-$) is shown in Fig. 13a. The ground state and excited state charge densities are modeled as point charges on the molecular centers and are provided elsewhere [73]. We define the excluded volume to be spheres centered at each atom in the molecule, with radii corresponding to the sum of that atom's van der Waals radius and the approximate radius of a water molecule ($r = 1.3$ Å). This represents the distance of closest approach of a solvent molecule's center of mass to the solute.

We reconstructed the dynamical hydration structure around the model C343$^-$ molecule using the density response function from IXS experiments as described in the previous section. The molecule is defined to be in its ground state and equilibrated with the surrounding hydration environment. Figure 13b depicts the induced oxygen density surrounding the C343$^-$ as a red isosurface. The strong hydration structure resides near two strongly charged oxygen atoms. Very little is induced near the hydrophobic, carbon dominated part.

For this reconstruction, the C343$^-$ is excited by changing its charge density to that for the excited molecule. The excluded volume is assumed to be constant. Figure 13c shows the change in molecular charge δq, with yellow patches signifying an increase in atomic charge and green a decrease. The size of the patches reflects the magnitude of charge change. The excited state reflects a reorganization of roughly 10% of the total charge to the middle of the molecule, inducing a hydrophilic patch there. This is seen qualitatively in the difference plot of the equilibrium ground state hydration structure n_{gs} and the equilibrium excited state hydration structure n_{exc} in Fig. 13d. The red surface represents an accumulation of additional water oxygen density in the excited state, while the blue represents a depletion. Qualitatively, water density shifts to hydrate the newly hydrophilic portion of the molecule.

The excitation and relaxation of the coumarin molecule serves as a probe of the hydration reorganization, as shown in Fig. 14. An equilibrated, ground state C343$^-$ molecule is excited at $t = 50$ fs. The response is tracked quantitatively
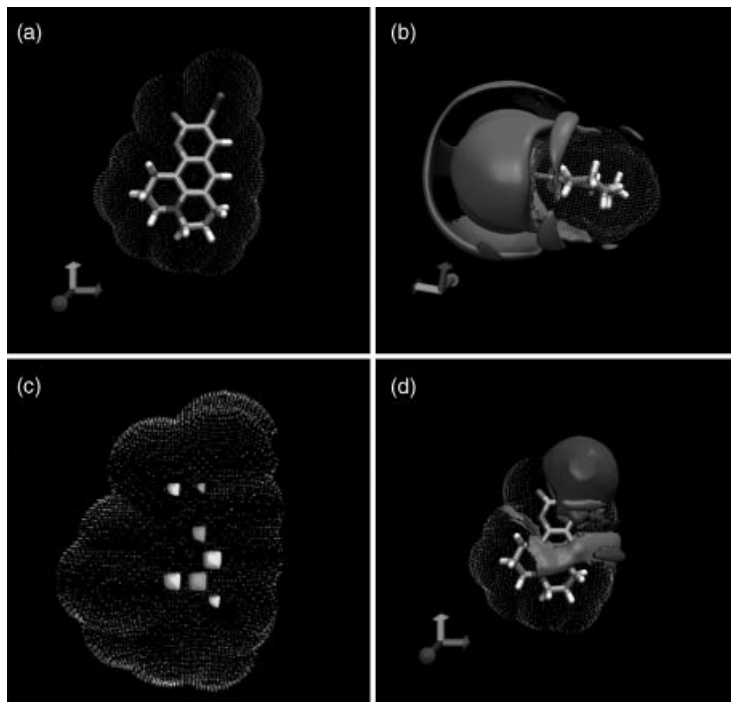
Figure 13. As an example, we show the hydration structure changes surrounding a model chromophore sequentially excited from, then relaxing to, its ground state charge structure. (**a**) The atomic structure of the coumarin-343 anion (C343⁻) [73]. A model for the ground state and excited state charge densities is also provided in that reference. The excluded volume (dotted isosurface) is defined as the sum of spheres centered at each atomic coordinate. The radius of each sphere is defined by the van der Waals radius of the underlying atom plus the approximate van der Waals radius of a water molecule (1.3 Å), indicating the distance of closest approach for a solvent water molecule's center of mass to the solute. (**b**) The hydration structure surrounding a C343⁻ molecule in its ground state. The solid isosurface represents the accumulation of water oxygen density. (**c**) When the molecule is excited, charge is transferred across the center of the molecule. The charge change δq is shown here, with increasing charge ($\delta q > 0$ for the atom) designated by white and reduced charge ($\delta q < 0$) as gray. The diameter of the patch indicates the magnitude of δq, with the largest patch representing roughly a 10% charge change. (**d**) The excited C343⁻ molecule induces a shift in the surrounding hydration structure from the ground state. Water oxygen is accumulated around the center of the molecule and depleted from the end that dominates the ground state hydration in (**b**). The isosurfaces here represent a 20% change in density from those in (**b**).

by measuring the deviation of the dynamical induced charge density $n_{ind}(t)$ from n_{gs}, $\langle (n_{ind}(t) - n_{gs})^2 \rangle$. For simplicity, we normalize this quantity by the deviation of the end points of the reconstruction, $\langle (n_{exc} - n_{gs})^2 \rangle$. If the deviation is zero, $n_{ind}(t) = n_{gs}$. If it is unity, $n_{ind}(t) = n_{exc}$.
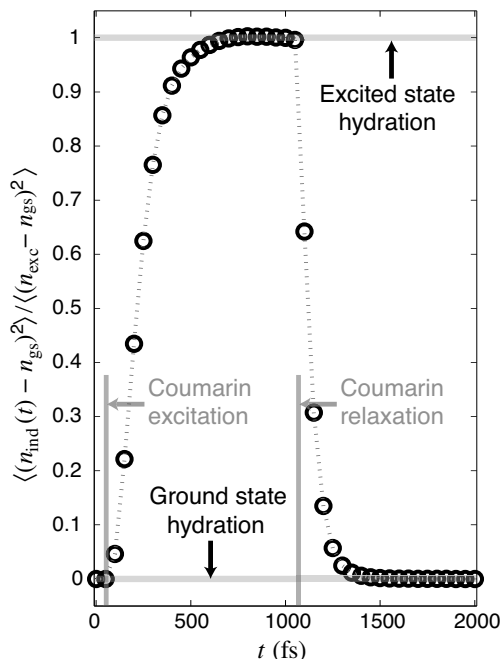
Figure 14. A hydrated ground state C343$^-$ molecule is excited ($t = 50$ fs), and the surrounding hydration responds to the change in the solute charge density. The deviation of the dynamical hydration structure $n_{ind}(t)$ from n_{gs}, the equilibrium hydration structure surrounding the ground state charge density, is plotted as a function of time. This deviation is normalized by the deviation of n_{exc}, the equilibrium hydration structure surrounding the excited state charge density, from n_{gs}. When the normalized deviation is equal to zero, $n_{ind}(t)$ is equivalent to n_{gs}. When the deviation is unity, $n_{ind}(t)$ is equivalent to n_{exc}. From the plot of the deviation for $t < 1000$ fs, the solvent responds to the excitation of the solute. The induced density rapidly responds to changes in the solute's charge density on a timescale of the order of a few hundred femtoseconds. When the molecule relaxes to its ground state ($t = 1050$ fs), the same 100 fs timescale is observed in the deviation response of the solvent. These timescales observed using GFID agree with those measured for the center of mass reorganization of water around small photoexcited solutes [25].

From Fig. 14, the solvent rapidly reorganizes in response to the solute charge density change. This occurs on the timescale of 200 fs and is complete after 700 fs. The rapid dynamics of center of mass reorganization is consistent with spectroscopic measurements of the hydration environment surrounding a real coumarin molecule [25]. We then relaxed the molecule by switching its charge density at $t = 1050$ fs and tracked the relaxation response. It occurred with identical dynamics to the excitation response, which is expected due to the linear response assumption.

This application of GFID demonstrates its capability for reproducing spectroscopic measurements by using the measured bulk response function with the same femtosecond resolution limitations. More important, it is able to *simultaneously* reconstruct the three-dimensional hydration structures with sub-Å spatial resolution. This combination of spatial and dynamical resolution gives GFID the capability to probe any number of systems that are currently infeasible for other experimental techniques.

3.   *Hydration of a Surface with Time-Independent Excluded Volume*

We use the above protocol for implementing excluded volume in polarizable media to reconstruct hydration near solid surfaces. It is important to note that although the surface structuring of the first water layer near this perfect abstract surface is smoother than that near real surfaces, the dynamics of subsequent hydration layers are described by the measured water–water interactions contained in the Green's function from inelastic X-ray scattering. We examine the hydration structure of a surface with a single embedded dipole. Each dipole is composed of charges q separated by $d = 2$ Å, centered at $y_0 = 2$ Å below the solid–water interface, and oriented so that the dipole moment is normal to the interface. The hydration structure near the solid surface is reconstructed from the bulk response function using the FFT-based methods described previously. An example of the 3D hydration structures is shown in Fig. 15, which also depicts the projection of the density onto the x–z plane. In contrast to the isotropic spherical shell of the hydration structure of a point charge, the hydration structure of a surface with a single dipole can be represented as a hydration "cap" or "umbrella," due to the existence of excluded volume interactions. In addition, this is oxygen density immediately adjacent to the solid surface. This density contains information on submolecular variations of oxygen density in the surface adhesive water and is commonly seen in simulations. To see this more clearly, the 3D hydration structure of water near the solid surface can be dissected as a z stack of 1 Å integrated layers (Fig. 15). Slice 1 shows density accumulation directly adjacent to the surface, indicating strong interactions between water and the dipole surface. Slices 2 and 3 show the first hydration shell. Density perturbations in layers for increasing z are diminished (slices 4 and up). Generalization of this technique for surfaces with more complex charge distributions can make contact with problems ranging from the no-slip boundary condition to nanoconfined water.

D.   Discussion

To intuitively describe the excluded volume implementation, one must first think of the boundary-free case. In Eq. (36), the solvent is treated as a continuous dielectric media for which the nonlocal properties and dynamics are determined by the response function. The solute is represented by an external charge distribution
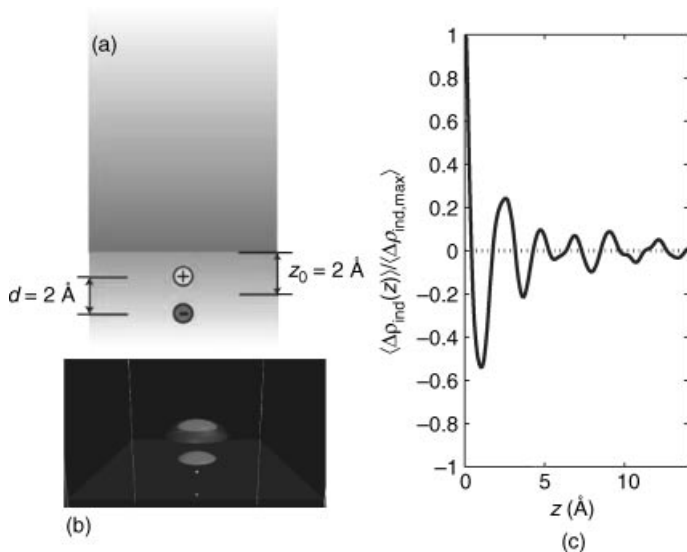
Figure 15. (**a**) A dipole embedded in a solid surface, with geometric parameters used in the GFID reconstruction. (**b**) An induced density isosurface for a dipole site embedded in a solid surface ($+q$ and $-q$). The light blue surface represents the cutoff for the excluded volume of the sheet. The solid density isosurfaces indicate the local accumulation of water oxygen. Note that the isotropic hydration shell of point charges has changed into a hydration "cap" in response to the excluded volume. (**c**) 1 Å integrated slices from the hydration structures of the single dipole in panel (**b**) (bottom is adjacent to surface, ordered going up with increasing distance from the surface, black bar represents 1 Å along the vertical axis). Water density can be found near the dipole position, indicating an adhesive layer that becomes part of the surface. Just above this are the first hydration shells of adhered water.

embedded in the dielectric. The polarization induced by the charge distribution at a particular point depends on the distribution's electric displacement over all space. Mathematically, the induced polarization is the convolution between the displacement and the dielectric tensor. The excluded volume implementation described here is a simple correction to the boundary-free case. It is a cavity in which the dielectric tensor is uniformly zero ($\epsilon = 1$) surrounded by solvent that responds according to the measured bulk properties. At a point outside the excluded volume, the polarization induced is the same as in the pure case, minus the contribution from the excluded volume. In essence, the excluded volume is carved out of the dielectric, with its contribution to screening the induced polarization elsewhere removed. The boundary defines where the solvent is permitted and where it is not.

This implementation lends itself immediately to systems in which the charge density is dynamical while the excluded volume is constant. An example of this is an infinite 2D charged sheet. Moving the sheet with a velocity parallel to the

plane of the sheet will cause a time-dependent displacement field that interacts with the solvent, but leaves the impenetrable boundary constant. Generalization of the present approach to account for dynamic excluded volumes is nontrivial. A more sophisticated implementation of excluded volume might require an approach that combines the density and polarization fields into a single description.

V. CONCLUSIONS AND OUTLOOK

As shown in the examples from Section IV.C, it is possible to reconstruct the hydration structure surrounding model solutes with excluded volume from meV IXS data. It is important to address the range of validity of this technique. For example, what are the physical limitations on the range of systems that can be studied using this technique? Linear response theory is believed to hold for most cases of physical solute–solvent systems, but it has been recently demonstrated to sometimes fail for cases involving chemical reactions and photoexcitation in various solvents [74–76]. A direct comparison between linear response in optical spectroscopies and in GFID is complicated by inherent differences in the underlying measured quantities. The physical mechanisms of linear response breakdown should be addressed before discussing them in the context of the specific linear response formalism in GFID.

The assumption of LR is that for small changes in solute charge density, the solvent relaxes through the same modes that govern density fluctuations at equilibrium. There are obviously physical situations in which LR fails to accurately describe hydration. An example of this is the solvent dynamics around positive and negative ions. In LR, exchanging a negative ion of identical valence for a positive one should result in a hydration structure that is identical in magnitude but opposite in sign. The asymmetric charge structure of water causes more substantial hydration differences between anions and cations than a simple sign inversion. LR is said to break down when this assumption does not hold. Recent experiments and computational models have become sophisticated enough to test the limits of LR. Several examples of LR breakdown have been demonstrated, where symmetric changes in the parameters of an experiment result in qualitatively different relaxation responses from the system. Recent examples of LR breakdown typically fall into two general mechanisms. The first is that upon excitation, the solute changes size. This affects the steric state as well as the energetics of hydration, rather than just the latter [74], causing a breakdown of LR. Similar systems show an asymmetric relaxation between the photoexcited cationic and anionic states of sodium [76]. The second type occurs when the solute changes so rapidly that it breaks the LR assumption of continuous solute–solvent interaction. For example, a CN molecule can maintain its angular velocity for many periods after photoexcitation, rather than continuously losing rotational energy to the environment, as it would under LR [75].

Systems with time-dependent excluded volume comprise a special class of problem. Although it might provide reasonable results, defining a time-dependent boundary according to the conditions specified in Section IV is incorrect. A dynamical excluded volume enforces an instantaneous rearrangement of solvent density and is unphysical. Furthermore, the induced polarization is subject to special treatment inside the cavity. It is explicitly set to zero. There is no way to enforce that the *particle density* is zero, so the excluded volume is indiscernible from *zero induced polarization*. It is clear from this consideration that to study a system with the present implementation of excluded volume, it must have a constant boundary. Physically relevant systems within this restriction include shearing infinite planar sheets or cylinders and molecular excitations inside of spheres, where the external charge densities move inside of excluded volume.

More sophisticated excluded volume treatments will be required to allow a dynamical excluded volume. An attempt based on this implementation could include defining the cavity as the phenomenologically determined, time-dependent combination of the initial and final cavity states. The chosen combination dynamics could be determined from arguments involving the self-diffusion constant of water or molecular dynamic simulations. This approach would still not be able to discriminate between its regions of excluded volume and zero induced polarization, however. A rigorous treatment requires the particle density and the electrostatic interactions to be treated simultaneously, similar to a dynamical version of the approach Beglov and Roux used for electrostatic solutes in water [77], or techniques based on the general Langevin equation [9]. Both approaches treat particle density and induced charge density separately and simultaneously. The first considers the solvent as a continuous dielectric as it has been throughout this section, while the second involves using interaction site models to describe the solvent and would allow the enforcement of solvent molecule granularity.

Having outlined the limitations, the GFID approach can have broad utility for many contexts. There are many physical systems for which simultaneous access to femtosecond dynamic information and sub-Angstrom spatial information can be illuminating. The dynamics of small volumes of water confined in nanometer channels simultaneously influences as well as gets influenced by the chemistry of the confining walls. Examples of this include "nanorheometers" composed of charged mica sheets and hydrophobic carbon nanotubes used in nanofluidic devices. The chemical composition of the channels and introduction of impurities can be freely studied in GFID, which can guide the design of novel nanoscale devices.

GFID might also be used to improve the efficiency and accuracy of molecular dynamics calculations. As described earlier, there is no universal model of water. Combining a "local" layer of molecular water with a large-scale water description based on the measured response function of water would improve the accuracy and efficiency of simulations. The measured response function captures the empirical

charge dynamics of water and would respond more accurately to the molecular motions in the system. The use of Green's function reduces the number of molecular degrees of freedom and the size of the MD "water box," which can result in speedup of the simulation. Direct method versions of GFID (rather than FFT-based calculations) might also be used to eliminate the need for periodic boundary conditions.

As the quality of $S(q, \omega)$ measurements improves, the density–density response function could potentially be used to generate newer models of water itself. The charge density of a water molecule in bulk simulations could be systematically optimized to match the simulated density response to the measured one. Similarly, GFID could potentially be paired with a molecular dynamics description of granular molecules to recover the effects of diffusion in charge reorganization. One potential approach might be to use Monte Carlo calculations to find molecular configurations of water that best fit the induced hydration structure calculated through GFID.

A more ambitious implementation of GFID could include iteration to allow the solute and solvent charge structures to "interact" in a self-consistent way. One could calculate the solvent structure around a given solute charge density. Density functional theory can then be used to calculate the solute structure, given the solvent structure. The procedure can be iterated, using the calculated solute structure as the next procedural input, until a predefined measure of convergence is reached. This can be extended to solute dynamics either by "exciting" the solute molecule or by parameterizing the nuclear coordinates, for example, and calculating a self-consistent solute–solvent structure at each time step. Using this approach, the measured response function can be used to improve dielectric solvent models for quantum chemistry calculations of solute electron density.

References

1. P. J. Feibelman, *Phys. Today*, **63**, 34 (2010).

2. Y. Zhu and S. Granick, *Phys. Rev. Lett.*, **87**(9), 096104 (2001).

3. T.-D. Li, J. Gao, R. Szoszkiewicz, U. Landman, and E. Riedo, *Phys. Rev. B*, **75**(11), 115415 (2007).

4. U. Raviv, P. Laurat, and J. Klein, *Nature*, **413**(6851), 51–54 (2001).

5. U. Raviv and J. Klein, *Science*, **297**(5586), 1540 (2002).

6. A. Poynor, L. Hong, I. K. Robinson, S. Granick, Z. Zhang, and P. A. Fenter, *Phys. Rev. Lett.*, **97**(26), 266101 (2006).

7. J. P. R. Day and C. D. Bain, *Phys. Rev. E*, **76**(4), 041601 (2007).

8. S. Chattopadhyay, A. Uysal, B. Stripe, Y.-G. Ha, T. J. Marks, E. A. Karapetrova, and P. Dutta, *Phys. Rev. Lett.*, **105**(3), 037803 (2010).

9. F. Hirata, ed., *Molecular Theory of Solvation*, Kluwer Academic Publishers, 2003.

10. K. D. Collins and M. W. Washabaugh, *Q. Rev. Biophys.*, **18**(4), 323–422 (1985).

11. S. K. Pal, J. Peon, and A. H. Zewail, *Proc. Natl. Acad. Sci. USA*, **99**(4), 1763–1768 (2002).

12. J. Israelachvili and H. Wennerström, *Nature*, **379**, 219–225 (1996).

13. F. Chiti, P. Webster, N. Taddei, A. Clark, M. Stefani, G. Ramponi, and C. M. Dobson, *Proc. Natl. Acad. Sci. USA*, **96**(7), 3590–3594 (1999).

14. A. H. Narten and H. A. Levy, *J. Chem. Phys.*, **55**(5), 2263–2269 (1971).

15. T. Head-Gordon and G. Hura, *Chem. Rev.*, **102**(8), 2651–2670 (2002).

16. A. K. Soper and M. G. Phillips, *Chem. Phys.*, **107**(1), 47–60 (1986).

17. Ph Wernet, D. Nordlund, U. Bergmann, M. Cavalleri, M. Odelius, H. Ogasawara, L. A. Naslund, T. K. Hirsch, L. Ojamae, P. Glatzel, L. G. M. Pettersson, and A. Nilsson, *Science*, **304**(5673), 995–999 (2004).

18. J. D. Smith, C. D. Cappa, K. R. Wilson, B. M. Messer, R. C. Cohen, and R. J. Saykally, *Science*, **306**(5697), 851–853 (2004).

19. A. K. Soper and J. L. Finney, *Phys. Rev. Lett.*, **71**(26), 4346 (1993).

20. A. Filipponi, D. T. Bowron, C. Lobban, and J. L. Finney, *Phys. Rev. Lett.*, **79**(7), 1293 (1997).

21. L.-A. Naslund, D. C. Edwards, P. Wernet, U. Bergmann, H. Ogasawara, L. G. M. Pettersson, S. Myneni, and A. Nilsson, *J. Phys. Chem. A*, **109**(27), 5995–6002 (2005).

22. S. Woutersen, U. Emmerichs, and H. J. Bakker, *Science*, **278**(5338), 658–660 (1997).

23. M. L. Cowan, B. D. Bruner, N. Huse, J. R. Dwyer, B. Chugh, E. T. J. Nibbering, T. Elsaesser, and R. J. D. Miller, *Nature*, **434**(7030), 199–202 (2005).

24. C. J. Fecko, J. D. Eaves, J. J. Loparo, A. Tokmakoff, and P. L. Geissler, *Science*, **301**(5640), 1698–1702 (2003).

25. R. Jimenez, G. R. Fleming, P. V. Kumar, and M. Maroncelli, *Nature*, **369**(6480), 471–473 (1994).

26. M. F. Kropman and H. J. Bakker, *Science*, **291**(5511), 2118–2120 (2001).

27. S. Park and M. D. Fayer, *Proc. Natl. Acad. Sci. USA*, **104**(43), 16731–16738 (2007).

28. G. Ruocco, F. Sette, U. Bergmann, M. Krisch, C. Masciovecchlo, V. Mazzacurati, G. Signorelli, and R. Verbeni, *Nature*, **379**(6565), 521–523 (1996).

29. F. Sette, G. Ruocco, M. Krisch, U. Bergmann, C. Masciovecchio, V. Mazzacurati, G. Signorelli, and R. Verbeni, *Phys. Rev. Lett.*, **75**(5), 850–853 (1995).

30. F. Sette, G. Ruocco, M. Krisch, C. Masciovecchio, R. Verbeni, and U. Bergmann, *Phys. Rev. Lett.*, **77**(1), 83–86 (1996).

31. P. Abbamonte, K. D. Finkelstein, M. D. Collins, and S. M. Gruner, *Phys. Rev. Lett.*, **92**(23), 237401 (2004).

32. G. Ruocco and F. Sette, *J. Phys. Condens. Matter*, **11**(24), R259–R293 (1999).

33. W. Schulke, Inelastic scattering by electronic excitations. *Handbook on Synchrotron Radiation*, Vol. 3, Elsevier, Amsterdam, 1991.

34. S. K. Sinha, *J. Phys. Condens. Matter*, **13**(34), 7511–7523 (2001).

35. B. Dorner and H. Peisl, *Nucl. Instrum. Methods Phys. Res.*, **208**(1–3), 587–592 (1983).

36. D. Pines and P. Nozieres. *The Theory of Quantum Liquids*, Vol. 1, W. A. Benjamin, Inc., Reading, MA, 1966.

37. P. M. Chaikin and T. C. Lubensky, *Principles of Condensed Matter Physics*, Cambridge University Press, Cambridge, UK, 1995.

38. E. Burkel, *J. Phys. Condens. Matter*, **13**(34), 7627–7644 (2001).

39. A. Guinier, *X-Ray Diffraction: In Crystals, Imperfect Crystals, and Amorphous Bodies*, Dover Publications, New York, 1994.

40. C. Kittel. *Introduction to Solid State Physics*, 8th ed., Wiley, New York, 2004.

41. N. W. Ashcroft and N. D. Mermin, *Solid State Physics*, Holt, Rinehart and Winston, New York, 1976.

42. A. V. Okhulkov, Y. N. Demianets, and Y. E. Gorbaty, *J. Chem. Phys.*, **100**(2), 1578–1588 (1994).

43. G. Baym, *Lectures on Quantum Mechanics*, Westview Press, New York, 1974.

44. J. P. Hansen and I. R. McDonald, *Theory of Simple Liquids*, 3rd ed., Academic Press, Burlington, MA, 2006.

45. F. Sette, G. Ruocco, M. Krisch, C. Masciovecchio, and R. Verbeni, *Phys. Scr.*, **T66**, 48–56 (1996).

46. G. Ruocco, F. Sette, M. Krisch, U. Bergmann, C. Masciovecchio, and R. Verbeni, *Phys. Rev. B*, **54**(21), 14892 (1996).

47. F. Bencivenga, A. Cunsolo, M. Krisch, G. Monaco, G. Ruocco, and F. Sette, *J. Chem. Phys.*, **130**(6), 064501 (2009).

48. C. Masciovecchio, G. Ruocco, F. Sette, M. Krisch, R. Verbeni, U. Bergmann, and M. Soltwisch, *Phys. Rev. Lett.*, **76**(18), 3356 (1996).

49. F. Sette, M. H. Krisch, C. Masciovecchio, G. Ruocco, and G. Monaco, *Science*, **280**(5369), 1550–1555 (1998).

50. S. H. Chen, C. Y. Liao, H. W. Huang, T. M. Weiss, M. C. Bellisent-Funel, and F. Sette, *Phys. Rev. Lett.*, **86**(4), 740 (2001).

51. Y. Liu, D. Berti, P. Baglioni, S.-H. Chen, A. Alatas, H. Sinn, A. Said, and E. Alp, *J. Phys. Chem. Solids*, **66**(12), 2235–2245 (2005).

52. T. E. Angelini, R. Golestanian, R. H. Coridan, J. C. Butler, A. Beraud, M. Krisch, H. Sinn, K. S. Schweizer, and G. C. L. Wong, *Proc. Natl. Acad. Sci. USA*, **103**(21), 7962–7967 (2006).

53. R. H. Coridan, N. W. Schmidt, G. H. Lai, R. Godawat, M. Krisch, S. Garde, P. Abbamonte, and G. C. L. Wong, *Phys. Rev. Lett.*, **103**(23), 237402 (2009).

54. P. Abbamonte, T. Graber, J. P. Reed, S. Smadici, C. L. Yeh, A. Shukla, J. P. Rueff, and W. Ku, *Proc. Natl. Acad. Sci. USA*, **105**(34), 12159–12163 (2008).

55. P. Mark and L. Nilsson, *J. Phys. Chem. A*, **105**(43), 9954–9960 (2001).

56. R. Li, Z. Jiang, F. Chen, H. Yang, and Y. Guan, *J. Mol. Struct.*, **707**(1–3), 83–88 (2004).

57. H. J. Bakker, M. F. Kropman, and A. W. Omta, *J. Phys. Condens. Matter*, **17**(45), S3215–S3224 (2005).

58. R. H. Coridan, N. W. Schmidt, G. H. Lai, and G. C. L. Wong, *J. Phys. Condens. Matter*, **21**, 424115 (2009).

59. J. Tomasi and M. Persico, *Chem. Rev.*, **94**(7), 2027–2094 (1994).

60. A. A. Kornyshev, A. I. Rubinshtein, and M. A. Vorotyntsev, *J. Phys. C: Solid State Phys.*, **11**(15), 3307–3322 (1978).

61. M. V. Basilevsky and D. F. Parsons, *J. Chem. Phys.*, **105**(9), 3734–3746 (1996).

62. B. Roux, H. A. Yu, and M. Karplus, *J. Phys. Chem.*, **94**(11), 4683–4688 (1990).

63. B Bagchi, *Annu. Rev. Phys. Chem.*, **40**(1), 115–141 (1989).

64. P. A. Bopp, A. A. Kornyshev, and G. Sutmann, *J. Chem. Phys.*, **109**(5), 1939–1958 (1998).

65. X. Song, D. Chandler, and R. A. Marcus, *J. Phys. Chem.*, **100**, 11954 (1996).

66. R. Mancinelli, A. Botti, F. Bruni, M. A. Ricci, and A. K. Soper, *J. Phys. Chem. B*, **111**(48), 13570–13577 (2007).

67. L. Perera and M. L. Berkowitz, *J. Chem. Phys.*, **100**(4), 3085–3093 (1994).

68. M.-H. Ho, M. L. Klein, and I.-F. W. Kuo, *J. Phys. Chem. A*, **113**(10), 2070–2074 (2009).

69. M. W. Schmidt, K. K. Baldridge, J. A. Boatz, S. T. Elbert, M. S. Gordon, J. H. Jensen, S. Koseki, N. Matsunaga, K. A. Nguyen, and S. Su, *J. Comput. Chem.*, **14**(11) (1993).

70. E. R. Nightingale, *J. Phys. Chem.*, **63**(9), 1381–1387 (1959).

71. J. C. Grossman, E. Schwegler, and G. Galli, *J. Phys. Chem. B*, **108**(40), 15865–15872 (2004).

72. G. Jones and M. A. Rahman, *J. Phys. Chem.*, **98**(49), 13028–13037 (1994).

73. X. Song and D Chandler, *J. Chem. Phys.*, **108**, 2594–2600 (1998).

74. M. J. Bedard-Hearn, R. E. Larsen, and B. J. Schwartz, *J. Phys. Chem. A*, **107**(24), 4773–4777 (2003).

75. A. C. Moskun, A. E. Jailaubekov, S. E. Bradforth, G. Tao, and R. M. Stratt, *Science*, **311**(5769), 1907–1911 (2006).

76. A. E. Bragg, M. C. Cavanagh, and B. J. Schwartz, *Science*, **321**(5897), 1817–1822 (2008).

77. D. Beglov and B. Roux, *J. Chem. Phys.*, **104**(21), 8678–8689 (1996).

78. E. Pontecorvo, M. Krisch, A. Cunsolo, G. Monaco, A. Mermet, R. Verbeni, F. Sette, and G. Ruocco, *Phys. Rev. E*, **71**(1), 011501 (2005).

79. G. Monaco, A. Cunsolo, G. Pratesi, F. Sette, and R. Verbeni, *Phys. Rev. Lett.*, **88**(22), 227401 (2002).

80. W. Humphrey, A. Dalke, and K. Schulten, *J. Mol. Graphics*, **14**(1), 33–38 (1996).